

# Light Nuclei near Neutron and Proton Drip Lines in the Relativistic Mean-Field Theory

G.A. Lalazissis<sup>1,4</sup>, A.R. Farhan<sup>2</sup>, M.M. Sharma<sup>2,3</sup>,

<sup>1</sup>Physik Department, Technische Universität München, Germany

<sup>2</sup>Physics Department, Kuwait University, Kuwait 13060

<sup>3</sup>Max Planck Institut für Astrophysik,  
D-85740 Garching bei München, Germany,

<sup>4</sup>Department of Theoretical Physics,  
Aristotle University of Thessaloniki,  
Thessaloniki 54006, Greece

March 1, 2018

## Abstract

We have made a detailed study of the ground-state properties of nuclei in the light mass region with atomic numbers  $Z=10-22$  in the framework of the relativistic mean-field (RMF) theory. The nonlinear  $\sigma\omega$  model with scalar self-interaction has been employed. The RMF calculations have been performed in an axially deformed configuration using the force NL-SH. We have considered nuclei about the stability line as well as those close to proton and neutron drip lines. It is shown that the RMF results provide a good agreement with the available empirical data. The RMF predictions also show a reasonably good agreement with those of the mass models. It is observed that nuclei in this mass region are found to possess strong deformations and exhibit shape changes all along the isotopic chains. The phenomenon of the shape coexistence is found to persist near the stability line as well as near the drip lines. It is shown that the magic number  $N=28$  is quenched strongly, thus enabling the corresponding nuclei to assume strong deformations. Nuclei near the neutron and proton drip lines in this region are also shown to be strongly deformed.

# 1 Introduction

The advent of radioactive beams and emergence of several facilities to produce these has provided a possibility to study the structure and properties of nuclei far away from those known to us so far [1, 2, 3, 4, 5]. These so-called "exotic" nuclei transcend the valley of stability and possess the extreme ratios of protons to neutrons on both the sides. An increase in each unit of isospin makes nuclei vulnerable to decay and consequently nuclei in the extreme domains of the periodic table are far short-lived. An access to these nuclei with a view to study their structure and properties poses a serious experimental challenge. At the same time, a comprehension of the nuclear properties in such areas is essential. Such regions of the periodic table are now becoming far more accessible to experimental studies [5]. A knowledge of the structure of these nuclei is expected to facilitate the understanding of the processes responsible for synthesis of heavy elements.

Numerous theories have so far been applied to study structure of nuclei. The shell model provides the essential backbone of the most of the approaches which are based upon the treatment of a nucleus within a mean field. Some of these approaches are based upon mean-field generated from the density-dependent Skyrme functional within the Hartree-Fock approach [6, 7]. Both the zero-range and finite-range forces are used. The computational ease has made the zero-range Skyrme Hartree-Fock approach a useful tool to discern properties of nuclei. The finite-range forces of the Gogny type has had only limited applications [8, 9] owing to the complicated handling of the associated functions and a longer computational time required. Both the zero-range and the finite-range forces have achieved their successes. Such studies have mostly been confined to nuclei closer to the stability line. Efforts are on way to employ these approaches also to ex-

tre regions of nuclei. The role of the spin-orbit interactions and consequently the shell effects in regions far away from the stability line are recently being discussed. The shell effects and their influence on nuclear properties about the drip line is an important question which needs to be addressed.

The relativistic mean-field (RMF) theory [10, 11, 12, 13] has recently proven to be a powerful tool to describe and predict the properties of nuclei. The outstanding problem of the anomalous kinks in the isotope shifts of Pb nuclei [14], which remained intractable for a long time, could be successfully resolved with in the RMF theory [15]. However, in our studies with the RMF theory a few subtle differences have emerged vis-a-vis the Skyrme approach. It is realized that the spin-orbit interaction in the RMF theory, which arises as a result of the Dirac-Lorentz structure of the nuclear interaction leads to an implicit density dependence of the spin-orbit potential. The issue of the isospin dependence of the spin-orbit interaction has also been raised recently [16, 17, 18]. An introduction of the isospin dependence in the spin-orbit channel, derived in a fashion analogous to the RMF theory seems to cure the problem of the density-dependent Skyrme approach [17]. Consequently, this feature taken from the RMF theory is successful in obtaining the anomalous kink in the isotopic shifts of Pb nuclei using the Skyrme approach. It remains to be seen how this modification of the Skyrme theory will fare for nuclei away from the stability line.

The RMF theory has shown its success in reproducing isotope shifts and deformation properties of nuclei in the rare-earth region [19]. The peculiar behaviour of the empirical isotopic shifts [20] of rare-earth nuclei as well as those of the well-known experimental data on the chains of Sr and Kr nuclei could be described successfully by Lalazissis and Sharma [21] for the first time. It is worth recalling that the Skyrme approach faced a difficulty in reproducing the isotope

shifts of Sr nuclei, whereby the method of generator coordinates was employed to tackle this problem [22, 23]. On the other hand, the RMF theory owes its success in providing a very good description of the isotopes shifts partly to better shell effects and in part to an improved description of the deformations of nuclei, which affect the isotope shifts accordingly. The RMF theory has also been extended to many deformed nuclei earlier in ref. [24, 25, 26] and it has been shown that its predictions compare favourably with the known properties. An extensive study of nuclei in the Sr region has been made recently in ref. [27]. Using the deformed RMF theory a fairly good representation of the experimental data has been obtained. In another approach based upon modification of meson masses with density, properties of Ne and Mg isotopes have been described using the deformed Hartree-Fock-Bogoliubov theory [28].

Nuclei close to neutron drip-line present an interest due to their relevance to r-process nucleosynthesis [29]. Nuclei relevant to the neutron-rich nucleosynthesis lie typically in the region of Zr (about  $Z=36-44$ ) and have an enormously large neutron excess. Such nuclei are expected to remain inaccessible to experiments for a foreseeable future. However, a knowledge of these nuclei is necessary in order to understand the nuclear abundances [30]. There exist several theoretical models and chiefly among them various mass models [31] which can predict the properties of nuclei close to the neutron drip lines. These extrapolations are based naturally upon the their respective Ansatz's which are fitted to obtain various sets of available nuclear properties about the stability line. The main emphasis is on a better reproduction of a large number of nuclear masses known over the periodic table. The Finite-Range Droplet Model (FRDM) [32] and the Extended Thomas-Fermi with Strutinsky Integral (ETF-SI) [33] are the best known mass models which are fitted exhaustively to a large body of nuclear data. In both these

mass formulae attempts have been made to obtain a best possible description of nuclear masses and deformation properties. It is, however, not clear whether it is possible to reproduce other nuclear properties such as isotope shifts and nuclear sizes within these models.

These mass models also extrapolate the properties of nuclei in the region of drip lines. It has been observed that the FRDM and the ETF-SI predict the binding energies of nuclei close to the neutron drip lines, both of which are indicative of stronger shell effects. In the RMF theory, the shell effects about the neutron drip line have also been investigated. It was shown by Sharma et al. [34, 35] that the shell effects near the neutron drip line in Zr isotopic chains remain strong. This was found to be in consonance with that predicted by the FRDM. In addition, many nuclei in this chain were observed to be deformed and the deformations obtained in the RMF theory were in very close agreement with those predicted by the FRDM. The relativistic mean-field theory has recently been extended by including the relativistic Hartree-Bogoliubov approach [36] which takes the particle continuum properly into account. Again, the results indicate strong shell effects near the neutron drip line.

Many nuclei close to the neutron drip line have been accessed experimentally (refer to the reviews [1, 2, 3, 4, 5] for more details). The drip line nuclei which are accessible to experiments at present lie in the low-mass region. Radioactive beams which could produce nuclei near drip line in the light-mass region are currently available. Constant improvements are being made in the techniques to produce nuclei far away from the stability line with a view to study the associated properties. In this paper we study the properties of nuclei in the light-mass region in the RMF theory. We have selected several isotopic chains from  $Z=10$  to  $Z=24$ . The nuclei included in these chains encompass both the neutron and the proton

drip lines. The calculations have been performed within an axially symmetric deformed configuration, the details of which are provided in the section below. We will discuss the results on the the nuclear sizes and nuclear deformations. A comparison of our results will be made with the available experimental data. We will also compare our predictions for the extreme regions with the predictions of the FRDM and ETF-SI, where available. We will discuss the salient features of our results in a broader perspective of the properties of nuclei about the drip lines. In the last section we provide a summary of our results.

## 2 Relativistic Mean-Field Theory

The starting point of the RMF theory is a Lagrangian density [10] where nucleons are described as Dirac spinors which interact via the exchange of several mesons. The Lagrangian density can be written in the following form:

$$\begin{aligned}
\mathcal{L} = & \bar{\psi}(i\rlap{\not{D}} - M)\psi + \frac{1}{2}\partial_\mu\sigma\partial^\mu\sigma - U(\sigma) - \frac{1}{4}\Omega_{\mu\nu}\Omega^{\mu\nu} + \\
& \frac{1}{2}m_\omega^2\omega_\mu\omega^\mu - \frac{1}{4}\mathbf{R}_{\mu\nu}\mathbf{R}^{\mu\nu} + \frac{1}{2}m_\rho^2\rho_\mu\rho^\mu - \frac{1}{4}F_{\mu\nu}F^{\mu\nu} \\
& g_\sigma\bar{\psi}\sigma\psi - g_\omega\bar{\psi}\boldsymbol{\omega}\psi - g_\rho\bar{\psi}\boldsymbol{\rho}\boldsymbol{\tau}\psi - e\bar{\psi}\mathbf{A}\psi
\end{aligned} \tag{1}$$

The meson fields included are the isoscalar  $\sigma$  meson, the isoscalar-vector  $\omega$  meson and the isovector-vector  $\rho$  meson. The latter provides the necessary isospin asymmetry. The bold-faced letters indicate the isovector quantities. The model contains also a non-linear scalar self-interaction of the  $\sigma$  meson :

$$U(\sigma) = \frac{1}{2}m_\sigma^2\sigma^2 + \frac{1}{3}g_2\sigma^3 + \frac{1}{4}g_3\sigma^4 \tag{2}$$

The scalar potential (2) introduced by Boguta and Bodmer [37] has been found to be necessary for an appropriate description of surface properties, although several variations of the non-linear  $\sigma$  and  $\omega$  fields have recently been proposed

[38].  $M$ ,  $m_\sigma$ ,  $m_\omega$  and  $m_\rho$  denote the nucleon-, the  $\sigma$ -, the  $\omega$ - and the  $\rho$ -meson masses respectively, while  $g_\sigma$ ,  $g_\omega$ ,  $g_\rho$  and  $e^2/4\pi = 1/137$  are the corresponding coupling constants for the mesons and the photon.

The field tensors of the vector mesons and of the electromagnetic field take the following form:

$$\begin{aligned}\Omega^{\mu\nu} &= \partial^\mu\omega^\nu - \partial^\nu\omega^\mu \\ \mathbf{R}^{\mu\nu} &= \partial^\mu\boldsymbol{\rho}^\nu - \partial^\nu\boldsymbol{\rho}^\mu - g_\rho(\boldsymbol{\rho} \times \boldsymbol{\rho}) \\ F^{\mu\nu} &= \partial^\mu\mathbf{A}^\nu - \partial^\nu\mathbf{A}^\mu\end{aligned}\tag{3}$$

The classical variational principle gives rise to the equations of motion. Our approach includes the time reversal and the charge conservation. The Dirac equation can be written as:

$$\{-i\alpha\nabla + V(\mathbf{r}) + \beta[M + S(\mathbf{r})]\} \psi_i = \epsilon_i\psi_i\tag{4}$$

where  $V(\mathbf{r})$  represents the *vector* potential:

$$V(\mathbf{r}) = g_\omega\omega_0(\mathbf{r}) + g_\rho\tau_3\rho_0(\mathbf{r}) + e\frac{1 + \tau_3}{2}\mathbf{A}_0(\mathbf{r})\tag{5}$$

and  $S(\mathbf{r})$  being the *scalar* potential:

$$S(\mathbf{r}) = g_\sigma\sigma(\mathbf{r})\tag{6}$$

the latter contributes to the effective mass as:

$$M^*(\mathbf{r}) = M + S(\mathbf{r})\tag{7}$$

The Klein-Gordon equations for the meson fields are time-independent inhomogeneous equations with the nucleon densities as sources.

$$\begin{aligned}\{-\Delta + m_\sigma^2\}\sigma(\mathbf{r}) &= -g_\sigma\rho_s(\mathbf{r}) - g_2\sigma^2(\mathbf{r}) - g_3^3(\mathbf{r}) \\ \{-\Delta + m_\omega^2\}\omega_0(\mathbf{r}) &= g_\omega\rho_v(\mathbf{r}) \\ \{-\Delta + m_\rho^2\}\rho_0(\mathbf{r}) &= g_\rho\rho_3(\mathbf{r}) \\ -\Delta A_0(\mathbf{r}) &= e\rho_c(\mathbf{r})\end{aligned}\tag{8}$$

The corresponding source terms are

$$\begin{aligned}
\rho_s &= \sum_{i=1}^A \bar{\psi}_i \psi_i \\
\rho_v &= \sum_{i=1}^A \psi_i^\dagger \psi_i \\
\rho_3 &= \sum_{p=1}^Z \psi_p^\dagger \psi_p - \sum_{n=1}^N \psi_n^\dagger \psi_n \\
\rho_c &= \sum_{p=1}^Z \psi_p^\dagger \psi_p
\end{aligned} \tag{9}$$

where the sums are taken over the valence nucleons only. It should also be noted that the present approach neglects the contributions of negative-energy states (*no - sea approximation*), i.e. the vacuum is not polarized. The Dirac equation is solved using the oscillator expansion method [39].

### 3 Details of Calculations

As most of the nuclei considered here are open shell nuclei, pairing has been included using the BCS formalism. We have used constant pairing gaps which are taken from the empirical particle separation energies of neighbouring nuclei. The centre-of-mass correction is taken into account by using the zero-point energy of a harmonic oscillator. For nuclei in the extreme regions, where nuclear masses are not known, we have used the prescription of Möller and Nix [40] to calculate the neutron and proton pairing gaps. Accordingly,

$$\Delta_n = \frac{4.8}{N^{1/3}} \Delta_p = \frac{4.8}{Z^{1/3}}$$

The number of shells taken into account is 12 for both the Fermionic and Bosonic wavefunctions. It should be noted that for convergence reasons 14 shells were also considered. It turned out, however, that the difference in the results



is negligible and therefore all the calculations reported in the present work were performed in a 12 shells harmonic-oscillator expansion.

In this paper we have used the force NL-SH. It has been shown that the force NL-SH provides excellent results [41] for nuclei on both the sides of the stability line. The appropriate value of the asymmetry energy of this force renders an adequate description of nuclei on both the neutron rich as well as on the proton rich sides. The parameters of the force NL-SH are:

$$M = 939.0 \text{ MeV}; m_\sigma = 526.059 \text{ MeV}; m_\omega = 783.0 \text{ MeV}; m_\rho = 763.0 \text{ MeV}; \\ g_\sigma = 10.444; g_\omega = 12.945; g_\rho = 4.383; g_2 = -6.9099 \text{ fm}^{-1}; g_3 = -15.8337.$$

Here  $g_2$  is in  $\text{fm}^{-1}$  and  $g_3$  is dimensionless.

## 4 Results and Discussion

### 4.1 Binding Energies

The total ground-state binding energies of nuclei obtained in the RMF calculations for various isotopic chains are shown in Tables 1 and 2. The results are obtained from the axially deformed RMF calculations with 12 oscillator shells using the force NL-SH. The binding energies from the mass models FRDM and ETF-SI are also shown for comparison wherever available. In the last column of the tables the experimental binding energies [42] of the known isotopes are given. The binding energies in the RMF are in good agreement with the empirical values. The quality of agreement is particularly good for nuclei which are proton rich or neutron rich. For nuclei close to the stability line a slight disagreement between the RMF predictions and the experimental values appears. This disagreement is about 1-2% for some chains. It is a bit exaggerated for S nuclei. For the isotopic chains of Ti and Cr the RMF binding energies show an overall excellent agreement with the empirical data. A comparison of the RMF predictions

in the unknown region with those of the FRDM shows that the two values show a general agreement for all the chains except for S and Ar. Agreement between the RMF and FRDM predictions for nuclei close to the proton and neutron drip lines is fair. Only for S and Ar nuclei near the neutron drip line, the RMF shows a slightly stronger binding than in the FRDM.

The predictions of ETF-SI are available only for a few nuclei for low  $Z$  chains such as Ne and Mg. For the other chains such as Si, S and Ar, the ETF-SI results available for nuclei on the neutron-rich side show that the level of agreement amongst the RMF, FRDM and ETF-SI is about the same, i.e., the ETF-SI predictions agree reasonably well with the RMF and FRDM. However, for the isotopic chains of Ti and Cr, the ETF-SI tends to underestimate the binding energies of nuclei close to the neutron drip line as compared to the RMF and the FRDM.

The RMF results on the binding energies of nuclei in the isotopic chains considered here show that the RMF theory is able to provide an overall description of the experimental binding energies. A good representation of the experimental binding energies was also observed for deformed nuclei in the isotopic chains of Sr, Kr and Zr [21] as well as in many rare-earth chains in our earlier work [19]. The results for a broad range of isospin which includes both the neutron drip and proton drip lines, where experimental data is not known, are consistent with the predictions of the FRDM. Thus, the RMF theory having only 6 effective parameters which are fitted only to a very limited number of nuclei describes much of the experimental binding energies consistently.

## 4.2 Nuclear Radii and Sizes

The *rms* charge and neutron radii obtained from the deformed relativistic mean-field calculations are shown in Figs. 1-2. The charge radii show a peculiar behaviour that light isotopes of all the chains shown in the above figures exhibit a higher charge radius as compared to their heavier counterparts. The charge radii assume a minimum value for some intermediate mass nuclei and it again increases for higher masses. This behaviour is akin to an inverted parabola as a function of mass. Such a feature is demonstrated commonly by nuclei in deformed regions (see the review by Otten [20] for details), whereby nuclei a few neutron number below the most stable nucleus possess a larger charge radius. This is especially exemplified by the Sr and Kr chains [43, 44] where the lighter isotopes have a bigger *rms* charge radius than the heavier ones. However, an increase in the charge radius for very neutron deficient nuclei stems from the protons in the outermost orbitals. These protons are extended into space and create a proton skin. This skin is subdued considerably due to the Coulomb barrier which tends to bind the protons more strongly.

The experimental charge radii [45] of several nuclei for each isotopic chain are shown by solid circles. It can be seen that the RMF predictions show a good agreement with the known experimental data. We also show in Figs. 1-2 the charge radii from the mass model ETF-SI for comparison. For Ne, Mg and Si only a few predictions from the ETF-SI are available. However, for the isotopic chains above S, ETF-SI values are available for the neutron-rich side. Above Ca, the predictions of the ETF-SI are available for isotopes on both the sides of the valley of stability. For nuclei close to the stability line, the ETF-SI results show a fair agreement both with the experimental and the RMF values. However, the ETF-SI results tend to overestimate the RMF results for the neutron-rich side,

whereas for the proton-rich side the ETF-SI predictions are smaller than the RMF predictions. This feature may be due to the difference in the isospin dependence of the spin-orbit potential in the RMF theory and the Skyrme Ansatz [17].

The neutron radii in Figs. 1-2 show an increasing trend with mass for all the isotopic chains. For highly neutron deficient (proton rich) nuclei the neutron *rms* radius is much smaller than the corresponding charge radius. This has the obvious implication that the neutron deficient nuclei possess an extended proton skin. This aspect will become clear in Figure 3 on the neutron skin thickness ( $r_n - r_p$ ).

The neutron radii exhibit a kink about the magic neutron numbers  $N=20$  and  $N=28$ . The kink at  $N=20$  is prominent for Ne, Mg and Si isotopes. It becomes weaker for heavier isotopic chains of S, Ar, Ti and Cr. In these chains a moderate kink appears at  $N=28$  due to its vicinity to the neutron drip line. The end of each isotopic chain in Figs. 1-2 depicts nuclei close to the neutron drip line. For these nuclei the neutron radii show a strong increase as a consequence of a large spatial extension of neutrons. This should imply an existence of neutron halos for nuclei close to the neutron drip line.

The curves for the neutron radii cross those for the charge radii, for all the isotopic chains, at a mass number which corresponds to a neutron number higher than proton numbers by 2 for light chains and about 4 for heavier chains. This difference can be explained in part by the fact that the charge radii presented are not just the proton radii but are convoluted for the finite size of protons. Secondly, the Coulomb repulsion extends the mean field of protons slightly beyond that of the neutrons.

For the isotopic chain of Ca, the neutron radii show an unusual parabolic behaviour between  $A=40$  ( $N=20$ ) and  $A=48$  ( $N=28$ ). Since the proton number

for Ca isotopes is a strong magic number, it seems to enforce a very strong N=28 magic shell thus leading to a significant reduction in the radius of  $^{48}\text{Ca}$  as compared to its lighter neighbours. This results in a strong kink in the neutron radius at N=28. Such a feature is not seen in other isotopic chains where the effect of the N=28 shell tends to diminish.

Fig. 3 shows the neutron skin thickness ( $r_n - r_p$ ) obtained from the RMF calculations for the isotopic chains from Z=10 to Z=24. All the isotopic chains considered here encompass nuclei close to the proton drip line as well as those close to the neutron drip line. For highly neutron deficient nuclides i.e. close to proton drip, the neutron skin thickness is negative. This symbolizes a proton skin in all these nuclei. On the other side i.e. for nuclei possessing a large number of neutron excess and which are close to the neutron drip line, a positive and large neutron skin can be easily seen. This is suggestive of a significant neutron halo in the extremely neutron-rich nuclei.

The figures show an interesting point about the difference in the magnitude of the proton and neutron skins. For a given proton excess i.e. (Z-N), the corresponding proton skin thickness is seen to be much larger than the neutron skin thickness for the same value of neutron excess (N-Z). This is obviously due to the Coulomb repulsion of protons. The Coulomb effect will also have a consequence that the proton drip line is expected to arise much faster in going away from the stability line than the corresponding neutron drip line.

The effect of shell closure in neutron skin-thickness can be seen easily in some nuclear chains. The prominent case of such an effect is visible in the Ca isotopes where strong kinks at N=20 and N=28 are present. In other isotopic chains such as with the lower atomic numbers (upper panel) the kinks at N=20 and N=28 are also to be seen. In these cases, the shell N=20 is strongly magic and some effect

of  $N=28$  is still present. In contrast, for nuclei in the lower panel, i.e., above  $S$ , the kink at  $N=28$  becomes minimal. This is attributed to a diminishing shell gap at  $N=28$  in these nuclei.

We show the neutron and proton density distributions of a few neutron rich isotopes in Fig. 4. The nuclei included are  $^{42}\text{Mg}$ ,  $^{56}\text{S}$  and  $^{80}\text{Cr}$ . All these nuclei are close to the predicted neutron drip line. Here the neutron density is in stark contrast to the corresponding proton density. The density of neutrons in the interior of the nuclei is larger as compared to the proton density and it extends considerably in space as compared to the proton density. This difference in the density distributions is a reminder of the possibility of a large neutron halo in nuclei near the neutron drip line.

In Fig. 5 we show the density distributions for a few nuclei near the proton drip line. We have selected the nuclei  $^{20}\text{Mg}$ ,  $^{26}\text{S}$  and  $^{40}\text{Cr}$  to demonstrate the effect of the proton-excess ( $Z - N$ ) on the density distributions. The central density of protons as well as the proton density at the surface, both exceed the corresponding neutron densities. The spatial extension of the proton density can also be seen in all the three cases. Examining the  $S_{2p}$  values of these, it can be said that all these nuclei are in the vicinity of the proton drip line. In particular, the proton-excess of  $^{20}\text{Mg}$  and  $^{26}\text{S}$  is only 4 and 6, respectively. Thus, due to the strong Coulomb repulsion only a moderate value of the proton-excess seems to suffice to create nuclei close to the proton drip line. This can be contrasted strongly with the nuclei near the neutron drip-line. The neutron-excess ( $N - Z$ ) required to produce the Mg and S nuclei close to the neutron-drip line amounts to about 16 and 24, respectively. These numbers are about a factor of 4 larger than the corresponding numbers for the proton-drip line. This difference demonstrates the strength of the Coulomb force which causes the proton drip line nuclei to

appear much closer to the stability line than the neutron drip line. An obvious consequence of this effect is the constraint on the magnitude or on the relative extension of the proton density vis-a-vis the neutron density. Thus, the proton halo in such nuclei is reduced considerably due to low values of the proton-excess.

### 4.3 The Separation Energies

The 2-neutron separation energies  $S_{2n}$  for all the isotopic chains are shown in Fig. 6. Each curve represents an isotopic chain. The 2-neutron separation energies for isotopic chains with a higher  $Z$  number start from a higher value. The  $S_{2n}$  values show the characteristic decrease with an increase in neutron number. For a reasonably large neutron number each curve approaches the vanishingly low  $S_{2n}$  values. This represents the onset of the neutron drip. Inevitably, the  $S_{2n}$  curves for low- $Z$  chains are rather short for the neutron-drip line to reach. This would make many of the drip nuclei accessible to future experiments. On the other hand, the curves for high- $Z$  isotopic chains become longer until the  $S_{2n}$  values approach a nearly vanishing value for an access to the neutron drip line. Thus, nuclei near the neutron drip line possess a large neutron excess.

In Fig. 7 we show the 2-proton separation energies  $S_{2p}$ . The curves are labelled by a neutron number which corresponds to a given isotonic chain. The lowest curve is for  $N=8$  and the highest one denoted by the dashed line is for  $N=38$ . The  $S_{2p}$  values show an usual decreasing trend as the proton number  $Z$  increases. For nuclides with low neutron number  $N$ , the  $S_{2p}$  curve approaches a vanishing value rather fast. This implies that the proton drip line in low  $N$  nuclides can be accessed more easily than would be the case for high  $N$  nuclides. For nuclides with higher number of neutrons, a relatively larger number of protons are needed for the proton drip. Translating this fact into the proton drip line for

each element ( $Z$ ), it can be seen that for a given  $Z$ , the point at which a  $S_{2p}$  curve reaches about zero value, gives its associated neutron number. It can be realized that the asymmetry between  $Z$  and  $N$  for proton drip is small for low  $Z$  elements and that this asymmetry increases only moderately for high  $Z$  elements. This is in contrast to the neutron drip line which occurs for large values of neutron excess. This point has also been elaborated above in Figs. 4 and 5.

#### 4.4 The Quadrupole Deformation

Nuclei in all the isotopic chains, except Ca, considered in this study are prone to being deformed. The quadrupole deformation  $\beta_2$  obtained from the axially deformed mean-field minimization are shown in Figs. 9 and 10. The numerical values of the quadrupole deformation  $\beta_2$  and the hexadecapole deformation  $\beta_4$  as obtained in the RMF theory with the force NL-SH are given in Tables 3-5. It is observed that some nuclei also show a secondary minimum in the energy. The corresponding deformation for the secondary minimum is given within parentheses. The results show that a large number of nuclei in these chains are highly deformed. Nuclei with prolate as well as oblate deformations are predicted.

Nuclei in the Ne and Mg chains are overwhelmingly prolate. In all the chains shown in Fig. 9, nuclei with  $N=8$  are manifestly spherical. It shows that the magic number  $N=8$  enforces a spherical shape on the mean-field irrespective of the associated proton number. Going away from  $N=8$ , nuclei in the Ne and Mg chain assume a highly prolate shape with  $\beta_2$  close to 0.40. As the shell closure  $N=20$  is approached, nuclei tend to sphericise. This effect can be seen in all the isotopic chains shown in Figs. 9 and 10 including  $^{32}\text{Mg}$  and  $^{36}\text{S}$  which are predicted to be spherical. Above  $N=20$ , the Ne and Mg nuclei take up highly prolate shapes in the RMF theory. In comparison, the Si isotopes undergo a sequence of shape



transitions spherical-prolate-oblate-spherical and again spherical-prolate-oblate in going from  $A=22$  ( $N=8$ ) to  $A=46$  ( $N=32$ ). On the other hand, in the S and Ar chains nuclei are changing shape between prolate and oblate at regular intervals in the neutron number. The highly neutron-rich nuclei close to the neutron-drip line are shown to take a well deformed oblate shape for Si, S and Ar.

In the chains of Si, S and Ar, it is noticed that the shape transition from a prolate to an oblate shape is shown to occur from  $N=12$  to  $N=14$ . Thus, an addition of a pair of neutrons to  $N=12$  tends to switch the shape of a nucleus from prolate to oblate. Such a transition is not shown for Ne and Mg isotopes. However, in these nuclei a well-deformed oblate shape which coexists with the prolate shape, is predicted at  $N=14$  in the RMF theory.

The S and Ar isotopes show several of prolate to oblate transitions. In contrast, Ti and Cr chains which have proton numbers above the strong magic number  $Z=20$ , are free from such prolate to oblate transitions except for a slightly oblate shape in the vicinity of  $N=36-38$ . On the whole, Ti and Cr nuclides are predominantly prolate with a succession of a few shape changes to a spherical one. The transitions to a spherical shape from a prolate one at regular intervals and the behaviour akin to a bridge is noteworthy for the Cr nuclei.

#### 4.4.1 Comparison with the Experimental Data

It is well known that nuclei in this region are very strongly deformed. Especially, in the low- $Z$  chains, nuclei assume shapes of unusual proportion. We compare the RMF predictions on the quadrupole deformation ( $\beta_2$ ) of nuclei with the available experimental data in Table 6. The experimental data have been taken from the compilation of  $\beta_2$  by Raman et al. [46] from the analysis of the  $BE(2)$  values. It is noticed from Table 6 that a few Ne nuclei take up a very large value of  $\beta_2$ . Such

a magnitude is inexplicable in the RMF theory and particularly within an axially deformed configuration we have adopted. Some of these nuclei are hypothesized to possess a triaxial shape in other models. We can not account for the triaxiality in the present work. On the other hand, for the Ne isotopes the RMF theory produces from moderate to strong deformations as in the traditional parlance. For  $^{20}\text{Ne}$ , the RMF deformation is low as compared to the experimental value. This difference is due to the complex nature of the potential-energy landscape for  $^{20}\text{Ne}$ . The RMF theory, however, comes close to the empirical value for  $^{22}\text{Ne}$ .

The quadrupole deformations of several Mg isotopes are described well in the RMF theory. The RMF theory underestimates the empirical values slightly. This is also the case for the Si isotopes. A few Si isotopes are predicted to be oblate in the RMF theory. A comparison of the RMF predictions with the data is not straightforward as the empirical values do not give the sign of the deformation.

A notable difference in the deformation appears for  $^{32}\text{Si}$ . It is predicted to be nearly spherical in the RMF theory, whereas the empirical data show that it has a  $\beta_2 = 0.34$ . The spherical nature of  $^{32}\text{Si}$  in the RMF can be understood in that the associated neutron number  $N=18$  lies very close to the magic number  $N=20$  which overpowers the shape. A similar instance is seen for  $^{40}\text{Ar}$  which appears as spherical in the RMF theory. All nuclei with  $N=20$ , such as  $^{36}\text{S}$  and  $^{38}\text{Ar}$  are explicitly spherical in the mean field.

Recently,  $\beta_2$  values for a few neutron-rich S and Ar isotopes have been inferred from the BE(2) measurements [47]. The nuclei  $^{38,40,42}\text{S}$  and  $^{44,46}\text{Ar}$  have been found to possess significant quadrupole deformations. The corresponding experimental values are shown in Table 6. It can be seen that the RMF theory provides  $\beta_2$  values which are very close to the experimental ones for the nuclei  $^{40}\text{S}$ ,  $^{42}\text{S}$  and  $^{44}\text{Ar}$ . However, The nuclei  $^{38}\text{S}$  and  $^{46}\text{Ar}$  come out as spherical in the

RMF theory, whereas experimentally these nuclei are shown to be reasonably deformed. On the other hand, for several other Ar isotopes, the RMF deformations are close to the empirical values. The RMF values also approach the empirical values for several other S isotopes.

Most of the Ti isotopes are predicted to be spherical in the RMF theory because of a strong influence from the magic number  $Z=20$ . However, the Cr nuclei which move away from the influence of  $Z=20$  are duly deformed in the RMF theory and there is a reasonably good agreement with the empirical values.

#### 4.4.2 Comparison with Mass Models

The predictions for quadrupole deformation  $\beta_2$  from the mass models FRDM and ETF-SI are also shown for comparison in Figs. 9 and 10. Results from ETF-SI are not available for Ne and Mg chains and are available only partly for the Si and S chains. For Ar, Ti and Cr chains predictions of both the mass models have been compared with the RMF results in Fig. 10.

The FRDM results for Ne, Mg, Si and S chains represent roughly the pattern predicted by the RMF theory. The FRDM predicts several oblate shape transitions for Ne and Mg nuclei. Taking into account the shape-coexistence in Ne and Mg isotopes, the RMF results would come close to the FRDM predictions. For Si and S chains, the trend of the FRDM results seems to agree with that of the RMF results. The differences, however, can be seen for very light ( $A=24-26$ ) Si isotopes which are predicted to be prolate in the RMF theory and shown to be oblate in the FRDM. Another difference in the RMF and FRDM predictions is for S nuclei ( $A=54-56$ ) close to the neutron drip line. Here, the shape of the nuclei is predicted to be close to spherical in the RMF theory, whereas the FRDM predicts a highly deformed prolate shape. The ETF-SI results on Si and S show

many similarities as well as a few differences with the RMF and FRDM results. For example, S isotopes with  $A=46-48$  are predicted to be prolate in the RMF and FRDM, whereas in the ETF-SI, these nuclei take up a well-deformed oblate shape.

In the RMF theory, the Ar nuclei change the shape between a prolate and an oblate one along the chain, whereas the nuclei in approaching the neutron drip-line assume a predominantly oblate shape. The FRDM results, on the other hand, predict that the low-mass as well as heavy-mass Ar isotopes are oblate and that nuclei in the middle of the chain take up spherical shape. In comparison, the ETF-SI results, follow largely the trend predicted by the RMF theory.

The Ti nuclei show a slightly different behaviour in the deformation properties. A large number of Ti nuclei are seen to be spherical. The vicinity of the proton number to the strongly magic number  $Z=20$  lends a spherical shape to many of the Ti isotopes. Some of the Ti isotopes are, however, deformed with a nominal deformation  $\beta_2$  between 0.10-0.15. Only the very light  $^{34}\text{Ti}$  nucleus is predicted to have  $\beta_2$  about 0.20. A comparison of the RMF results with the FRDM shows that both the RMF and FRDM predict a prolate deformation for  $^{34}\text{Ti}$ , although in FRDM the  $\beta_2$  value predicted for this nucleus is a factor of 2 more than that in the RMF.

There is at least one Ti nucleus which takes an oblate shape. The nucleus  $^{58}\text{Ti}$  ( $N=36$ ) has an oblate deformation  $\beta_2 \sim -0.10$ . Both the RMF and the FRDM predict an oblate shape for  $^{58}\text{Ti}$  with a very good agreement in the  $\beta_2$  values. For most of the other Ti isotopes, the FRDM predicts a predominantly spherical shape, which is in good agreement with the RMF results. The shape transition spherical-prolate-spherical from  $A=66$  to  $A=72$  in the RMF theory appears very closely also in the FRDM. Thus, there are various similarities in the predictions of

the RMF theory and the FRDM. The ETF-SI, on the other hand, predicts that most of the Ti isotopes should have a reasonably strong prolate deformation. This is at variance with the predictions of the RMF and the FRDM.

The  $\beta_2$  values for the Cr isotopes show a most remarkable feature in Fig. 10. In the RMF theory, the shape of the Cr nuclei changes between a spherical and prolate one rather periodically. The cusps representing such a behaviour in the RMF theory are partly reproduced in the ETF-SI and partly in the FRDM. The very light Cr isotopes ( $A=38-40$ ) close to the proton drip line are predicted to assume a highly deformed prolate shape ( $\beta_2 \sim 0.25 - 0.30$ ). Both the FRDM and ETF-SI also predict similar deformations. However, on adding a few pairs of neutrons to these nuclei, the FRDM shows a spherical shape for nuclei up to  $A=52$ . The ETF-SI results, on the other hand, show the undulations in the  $\beta_2$  values upto  $A=60$ , similar to the RMF predictions, however, without going to a spherical shape at  $A=44$  and  $A=52$  as against the RMF where these nuclei take up a spherical shape. Above  $A=60$ , there is a broad agreement between the RMF and the FRDM results, whereas the ETF-SI results go out of tune with the other results and predict highly prolate shapes between  $A=60-70$ . In this region, the RMF and the FRDM results show a shape transition prolate-spherical-prolate where the  $\beta_2$  value reaches the maximum ( $A=70$ ) of the cusp. At  $A=74$  and above, the RMF theory as well as the mass models all predict a similar behaviour. The nucleus  $^{74}\text{Cr}$  ( $N=50$ ) is predicted to be spherical in the RMF theory and is nearly spherical in the FRDM and ETF-SI. Nuclei above  $A=74$  are close to the neutron drip line. These nuclei ( $A=78-80$ ) are predicted to have a reasonably well-deformed prolate shape in the RMF. This is supported by the mass models. Thus, for the Cr chain, nuclei near the proton drip line as well as those near the neutron drip line are predicted to be prolate shaped in all

the three results presented in Fig. 10.

## 4.5 The Hexadecapole Deformation

The hexadecapole deformation  $\beta_4$  obtained in the RMF theory are shown in Tables 3-5. It is as per common expectation that  $\beta_4$  is zero for nuclei with spherical shapes (magic numbers). This is true for most magic numbers except for  $N=28$ . For nuclei with  $N=28$ , we observe that the  $\beta_4$  has a significant value for the Ne, Mg, Si and S isotopes as these nuclei possess a correspondingly large quadrupole deformation  $\beta_2$ . For Ar, Ti and Cr nuclei with  $N=28$ , however,  $\beta_4$  is close to zero as these nuclei are obtained to be spherical under the influence of the vicinity of  $Z=20$ . Clearly,  $\beta_4$  tends to vanish for all nuclei with a vanishing  $\beta_2$ .

Many nuclei in this region show strong hexadecapole deformation as given in Tables 3-5. In the Ne chain, most nuclei have a zero or a very small  $\beta_4$ . Here only the nucleus  $^{34}\text{Ne}$  is predicted to have a large and positive  $\beta_4$ . For the case of Mg isotopes, the  $\beta_4$  values predicted for most nuclei are also small or very moderate. In comparison, the FRDM predicts substantial hexadecapole deformation for several nuclei in the Ne and Mg chains. It can be noticed that  $\beta_4$  values for many strongly deformed (large  $\beta_2$ ) nuclei in the RMF are small. On the other hand, the  $\beta_4$  values in FRDM are proportionately larger for highly deformed nuclei. This situation with regard to  $\beta_4$  persists also for Si isotopes in the RMF theory vis-a-vis FRDM, with only an occasionally large  $\beta_4$  in RMF. For S isotopes, on the other hand, both the RMF and FRDM predict moderate values for  $\beta_4$ , with FRDM predicting a significantly large  $\beta_4$  only for a very few nuclei. As to the signs of the deformations, there seems to be a little correlation between the signs of  $\beta_2$  and  $\beta_4$  for nuclei in the Ne, Mg, Si and S chains. However,

most S isotopes show a negative  $\beta_4$  values in the RMF as well as in the FRDM.

The RMF theory predicts small  $\beta_4$  values for Ar, Ti and Cr nuclei as well. For the Ar chain, in comparison, the FRDM predicts strong hexadecapole deformation for many nuclei. A strong correlation between  $\beta_2$  and  $\beta_4$  is found for Ar nuclei. Both the RMF and FRDM predict a negative  $\beta_4$  for oblate nuclei. This is the case for neutron deficient as well as for neutron rich nuclei. As can be seen, most Ar nuclei are oblate deformed.

As one goes above  $Z=20$ , both the RMF and FRDM show small values of  $\beta_4$  for Ti and Cr chains. The FRDM, in addition, predicts a reasonably large  $\beta_4$  for a few Ti and Cr nuclei at the beginning or at the end of the chains. For other nuclei, there is a broad agreement between the RMF and FRDM on small values of the hexadecapole deformation for these isotopic chains.

The ETF-SI predictions for  $\beta_4$  are also shown in Tables 3-5. The ETF-SI values for  $\beta_4$  for the lighter chains are available only scantily. For heavier chains, the ETF-SI predictions are known for many nuclei. It may be remarked that by and large the ETF-SI values, where available, are in line with the RMF predictions of small  $\beta_4$ .

## 4.6 Shell Closures and Deformations

The nuclear structure and the ensuing shell effects associated to the magic numbers are important to understanding the relative abundances of nuclei. Nuclei are formed either through the neutron-rich nucleosynthesis or via rapid neutron capture (r-process). The existence of a major shell in the path of the neutron-rich nucleosynthesis or r-process provides a stability to the nuclei concerned and thus influences the abundance of the product nuclei. For example, the shell effects around Ca affect the synthesis of nuclei and their abundances in the region of

iron.

The shell closures encountered in the mass range we have studied appear at the particle numbers 8, 20, 28 and 50. Here we examine the predictions of the RMF theory along with those of the FRDM and ETF-SI for deformations at and in the vicinity of these magic numbers.

Some nuclei such as  $^{18}\text{Ne}$ ,  $^{20}\text{Mg}$  and  $^{22}\text{Si}$  included in Fig. 9 have the neutron number  $N=8$ . Most of these nuclei are highly deficient in neutrons and are close to the proton drip line. The results of the RMF theory on  $\beta_2$  show that all the above nuclei are predicted to be spherical. Thus, the magicity of  $N=8$  is retained also about the proton drip line. The corresponding results from the FRDM show that although the trend of the deformations of nuclei with neutron numbers above  $N=8$  are similar in the FRDM to those from RMF with a few exceptions, the FRDM is predicting a marginally prolate deformed nuclei for  $N=8$ . It is, however, not known how the ETF-SI predictions for the  $N=8$  magic number are ?

The next magic number  $N=20$  is considered to be a prominently strong shell closure. Calcium nuclei with  $Z=20$  are well-known to be strongly magic. All the isotopic chains considered here include nuclei with  $N=20$ . It can be seen from Figs. 9 and 10 that nuclei with  $N=20$  in all the isotopic chains are predicted to be spherical in the RMF theory. Thus, the strong shell closure at  $N=20$  sphericizes the total mean field. This feature is also to be seen in the predictions of the FRDM for all the chains from Ne to Cr. The ETF-SI results for  $N=20$  nuclides for Ne, Mg and Si are not available. The ETF-SI predictions for  $^{36}\text{S}$ ,  $^{38}\text{Ar}$  and  $^{42}\text{Ti}$  ( $N=20$ ) show that these nuclei are spherical.

Next, we consider properties of nuclei with the magic number 28. The nuclei with  $N=28$  included in Figs. 9 and 10 are  $^{40}\text{Mg}$ ,  $^{42}\text{Si}$ ,  $^{44}\text{S}$ ,  $^{46}\text{Ar}$ ,  $^{50}\text{Ti}$  and  $^{52}\text{Cr}$ . The RMF results show that the nuclei  $^{40}\text{Mg}$  ( $\beta_2 = 0.45$ ),  $^{42}\text{Si}$  ( $\beta_2 = -0.34$ ) and



$^{44}\text{S}$  ( $\beta_2 = -0.20$ ) are highly deformed. The nucleus  $^{44}\text{S}$  is oblate deformed in its lowest energy state in the RMF theory. However, for this nucleus there is a shape-coexistence of the oblate shape with a highly prolate shape ( $\beta_2 = 0.38$ ) which lies about 30 keV above. These two states are practically degenerate. Earlier, it was shown in [48] that the shape and deformation of a nucleus is very important to obtaining a correct  $\beta$ -decay probability. On the basis of the measured decay half-lives, it was surmised [48] that the ground-state of the nucleus  $^{44}\text{S}$  is oblate deformed. The oblate ground state for  $^{44}\text{S}$  in the RMF theory is consistent with this conclusion. However, it is not clear how much will be the influence of the prolate state on the  $\beta$ -decay probability.

The above examples serve to demonstrate that the shell closure  $N=28$  is very weak and that shell effects due to  $N=28$  are quenched. However, this may not be a general feature as the nuclei  $^{46}\text{Ar}$ ,  $^{50}\text{Ti}$  and  $^{52}\text{Cr}$  maintain a spherical shape. This may be due to a combined effect of the proton number, which is close to the magic number  $Z=20$ , and that of the shell closure at  $N=28$ , which lends a spherical symmetry to the mean field. Thus, the number  $N=28$  is not universally magic. Considering the results of the mass models, the FRDM shows a behaviour similar to the RMF theory in the quenching of the shell effects at  $N=28$  for Mg, Si and S nuclei. For the nuclei Ar, Ti and Cr (with  $N=28$ ) the FRDM shows that these nuclei take a spherical shape similar to that predicted by the RMF. Thus, for these nuclei the magicity of  $N=28$  is maintained also in the FRDM.

The ETF-SI predictions for  $N=28$  nuclei are available for isotopic chains heavier than Mg. It can be seen that the ETF-SI predicts a well-deformed shape for  $^{42}\text{Si}$  and  $^{44}\text{S}$ . This is in good accord with the predictions of the RMF and FRDM. However, the ETF-SI predicts a deformed shape also for  $^{46}\text{Ar}$ ,  $^{50}\text{Ti}$  and  $^{52}\text{Cr}$ , which are all predicted to be spherical both in the RMF and FRDM. Thus, the

ETF-SI maintains the quenching of the shell effects and leads to a considerable weakening of the magicity of  $N=28$  in all the above nuclei. The results of the ETF-SI for  $N=28$  nuclei are in a slight contrast with those of the RMF and the FRDM.

Shell closure at  $N=50$  has shown itself to be strong in the known nuclei. However, when it is stretched to the extreme regions, it is not known experimentally whether the magicity of  $N=50$  continues to persist. The only isotopic chains where nuclei with  $N=50$  could be constructed are those of Ti and Cr. The nuclei  $^{72}\text{Ti}$  and  $^{74}\text{Cr}$  with  $N=50$  are expected to lie close to the neutron drip line. It can be seen from Fig. 10 that Ti and Cr nuclei immediately below  $N=50$  are predicted to be prolate deformed in the RMF theory, the deformation being stronger for Cr nuclei. The Cr nuclei above  $N=50$  are also shown to take a prolate shape. However, the Ti and Cr isotopes with  $N=50$  do take up a spherical shape. Thus, the shell closure and the magicity of  $N=50$  near the neutron drip line is strong in the RMF theory. Both the FRDM and ETF-SI also predict a nearly spherical shape for nuclei with  $N=50$  near the neutron drip line, thus maintaining strong shell effects at  $N=50$ .

## 4.7 Neutron-Proton Deformations

As we have included long chains of several nuclei which encompass both the proton and neutron drip lines, the range of the variation in the isospin of the nuclei is considerably large. This provides a testing ground for the relative variation in the neutron mean-field vis-a-vis the proton mean-field as a function of the isospin. The position of both the proton and the neutron number of a nucleus from a closed shell is decisive to what shape the respective mean fields assume. From this point of view, it is illustrative to compare the deformations of the

neutron and proton mean-fields as a function of the isospin. In Figs. 11 and 12 we show the difference  $\beta_2(n) - \beta_2(p)$  in the quadrupole deformations of the neutron and proton fields.

For most of the Ne nuclei below  $A=26$ , which are deformed (see Fig. 9), the difference in the deformation of the neutron and proton densities is very small and close to zero except for the nucleus  $^{22}\text{Ne}$  which shows that the neutron mean-field is slightly more deformed than the proton mean field. Here the neutron number  $N=14$ , which lies in the middle of  $N=8$  and  $N=20$ , seems to produce more deformation for neutrons. Nuclei between  $A=26$  and  $A=32$  are spherical and hence the obvious value (zero) of  $\beta_2(n) - \beta_2(p)$ . An interesting aspect appears above  $A=32$ . The nuclei from  $A=34$  to  $A=38$  take up an increasingly larger  $\beta_2$  as the neutron number increases (Fig. 9). It can be seen from Fig. 11 that for these nuclei, the difference  $\beta_2(n) - \beta_2(p)$  also increases with an increase in the  $\beta_2$  value with a successive addition of a pair of neutrons. Thus, the additional neutrons to  $N=20$  core tend to drive the neutron matter to highly deformed shape as compared to the proton matter. This can be exemplified by stating that  $^{38}\text{Ne}$ , which shows a large deformation  $\beta_2 = 0.44$ , has  $\beta_2(n) = 0.49$  and  $\beta_2(p) = 0.32$ . Thus, there is a substantial difference between the deformations of the neutron and proton mean-fields.

Isotopes in the Mg chain, except  $^{32}\text{Mg}$  ( $N=20$ ), have been shown to possess a prolate shape in the RMF theory. The difference  $\beta_2(n) - \beta_2(p)$  is, however, shown to have a rather strange feature. The light Mg isotopes below  $N=20$  ( $A=32$ ) show a negative  $\beta_2(n) - \beta_2(p)$  and those above  $N=20$  have a positive  $\beta_2(n) - \beta_2(p)$ . This means that the light Mg isotopes with mass upto  $A=30$  ( $N=18$ ) have a more strongly deformed proton mean-field than the neutron mean-field. For example, the highly deformed nucleus  $^{22}\text{Mg}$ , which has a prolate deformation

$\beta_2 = 0.43$ , has  $\beta_2(p) = 0.46$  and  $\beta_2(n) = 0.39$ . Thus, proton number  $Z=12$  produces a stronger deformation than the neutron number  $N=10$ . For  $^{24}\text{Mg}$ , which has an equal number of protons and neutrons, such a big difference in the deformations is not apparent. However, for the nuclei  $^{26}\text{Mg}$  ( $N=14$ ) and  $^{30}\text{Mg}$  ( $N=18$ ), the difference in  $\beta_2(n) - \beta_2(p)$  is not insignificant and the deformation  $\beta_2(p)$  continues to be bigger than the corresponding  $\beta_2(n)$ . This shows that below  $N=18$  the deformation tendencies of  $Z=12$  are far stronger than those of any neutron number. The above effect is, however, taken over by the neutrons which play a leading role in deforming the nuclei beyond  $^{32}\text{Mg}$  ( $N=20$ ), noting that all nuclei above and including  $^{34}\text{Mg}$  are highly deformed ( $\beta_2 \sim 0.4$ ). One observes a positive  $\beta_2(n) - \beta_2(p)$  for nuclei. This difference increases to a considerable value of about 0.09 ( $\beta_2(n) = 0.48$  and  $\beta_2(p) = 0.39$ ) for  $^{40}\text{Mg}$  ( $N=28$ ). This shows that although the neutron number  $N=28$  constitutes the known shell-closure, the neutron mean-field take up a very large deformation and forces the nucleus to take a highly deformed shape ( $\beta_2 = 0.45$ ). Thus, the shell-closure at  $N=28$  is washed out and the shell effects are considerably weakened.

The Si nuclei from  $A=22$  ( $N=8$ ) to  $A=36$  ( $N=22$ ) do not show any marked difference in the deformations of neutrons and protons, though Si nuclei with large prolate as well as oblate deformations have been predicted in the RMF theory (see Fig. 9). However, for isotopes including and above  $A=38$  ( $N=24$ ),  $\beta_2(n)$  becomes larger than  $\beta_2(p)$ . Such a behaviour persists even across the shape transition from prolate to oblate at  $A=42$  (Fig. 9) and now the negative  $\beta_2(n)$  values are bigger than the negative  $\beta_2(p)$  values and hence a negative  $\beta_2(n) - \beta_2(p)$  as shown in Fig. 11. Thus, for heavier Si isotopes, a dominance of neutron deformation over the proton deformation is seen both for the prolate and the oblate nuclei, as opposed to the light Mg isotopes where the proton deformation overweighed against the

neutron deformation in the RMF theory.

The behaviour of S isotopes towards the difference  $\beta_2(n) - \beta_2(p)$  is similar to that of Si isotopes. Although the S nuclei show a variety of shape transitions throughout the isotopic chain, a closer look at the  $\beta_2(n) - \beta_2(p)$  values shows that for  $^{34}\text{S}$  (N=18) the  $\beta_2(p)$  is bigger than  $\beta_2(n)$ . This is due to the vicinity of N=18 to the magic number N=20, which enforces a less deformed neutron mean-field as compared to the proton mean-field. All the other S isotopes have, however, a higher neutron deformation than the proton deformation. This is the case for both the prolate and oblate shapes in the lowest minimum.

The case of  $^{44}\text{S}$  needs a special mention. This nucleus (N=28) has an oblate shape ( $\beta_2 = -0.20$ ) in the lowest minimum. However, a highly deformed prolate shape ( $\beta_2 = 0.38$ ) for this nucleus is almost degenerate (only 27 keV higher) with the oblate one. The neutron-proton difference in the deformation for the oblate shape is marginally low and is shown in Fig. 11. However, for the prolate shape a large difference  $\beta_2(n) - \beta_2(p) = 0.10$  ( $\beta_2(n) = 0.41$  and  $\beta_2(p) = 0.31$ ) is observed. It is interesting to note that notwithstanding the N=28 magic number, the neutron mean-field is susceptible (softer) to the stronger deformation than the proton mean-field.

The deformation curve ( $\beta_2$ ) for Ar isotopes in the RMF theory as shown in Fig. 10 seems to be reflected considerably in the difference  $\beta_2(n) - \beta_2(p)$  as shown in Fig. 12. Only for the nuclei  $^{32}\text{Ar}$  and  $^{36}\text{Ar}$  which show an oblate deformation (negative  $\beta_2$ ), the difference  $\beta_2(n) - \beta_2(p)$  is shown to be positive. This implies that for all the deformed Ar isotopes except these two nuclides, the neutron deformation  $\beta_2(n)$  exceeds the proton deformation  $\beta_2(p)$ . This is the case also for the oblate shaped nuclei. For example,  $^{52}\text{Ar}$  (N=34) which has an oblate deformation  $\beta_2 = -0.22$  has a  $\beta_2(n) = -0.24$  and  $\beta_2(p) = -0.19$ , with a

substantial difference of  $\beta_2(n) - \beta_2(p) \sim -0.05$ . Thus, also for the Ar isotopes, the neutron mean-field is more susceptible to deformation than the proton mean-field. This is due to the reason that the proton number  $Z=18$  being very close to the magic number  $Z=20$  lends itself to the spherical tendency.

The Ti isotopes also replicate the behaviour of their  $\beta_2$  values (Fig. 10) in the difference  $\beta_2(n) - \beta_2(p)$  as shown in Fig. 12, i.e. nuclei with a positive  $\beta_2$  have a positive difference  $\beta_2(n) - \beta_2(p)$  and those with a negative  $\beta_2$  have a negative  $\beta_2(n) - \beta_2(p)$ . The only exception is the nucleus  $^{34}\text{Ti}$  ( $N=12$ ) which has a quadrupole deformation  $\beta_2 \sim 0.21$  and the difference in the deformations of its neutron and proton densities is close to zero. For other deformed Ti nuclei, the differences  $\beta_2(n) - \beta_2(p)$  are proportional to the corresponding  $\beta_2$  values. However, the differences in the deformations of neutron and proton densities are moderate as compared to those found for some Ne and Mg isotopes and are found to be slightly smaller than those for some Si, S and Ar nuclei. This is due to the fact that Ti has a proton number  $Z=22$  which is close to the strongly magic number  $Z=20$ . Thus, the Ti isotopes oppose tendencies which would produce vigorous changes and differences in the neutron and proton deformations.

The behaviour of Cr isotopes for the  $\beta_2(n) - \beta_2(p)$  is very different as compared to all the other chains considered here. As discussed in the previous section, the Cr isotopes show a shape transition between prolate and spherical shapes periodically with the neutron number (Fig. 10). However, the most of the Cr isotopes ( $A=48-76$ ) show only an insignificant difference in the deformations of the neutron and proton mean fields, although the mean deformation of several Cr isotopes rises to about 0.20 or more (see Fig. 10). Only for very light Cr isotopes close to the proton drip line and for very heavy ones close to the neutron drip line, does  $\beta_2(n) - \beta_2(p)$  take a significant value. For  $^{38}\text{Cr}$  ( $N=14$ ) which has a mean

prolate deformation  $\beta_2 \sim 0.29$ , the proton deformation  $\beta_2(p)$  assumes the value  $\sim 0.32$  and the neutron deformation  $\beta_2(n)$  is only 0.23. Thus, the proton mean field is considerably more deformed than the neutron mean field and drives the nucleus to a highly deformed shape. Such an effect has not been seen for proton drip nuclei for other chains. It may, however, be noted that although being close to the proton drip line, the nuclei  $^{38}\text{Cr}$  and  $^{40}\text{Cr}$  are unbound in the RMF theory.

An interesting but less pronounced difference in the deformations can be observed for Cr nuclei close to the neutron drip line. The nuclei  $^{78}\text{Cr}$  (N=54) and  $^{80}\text{Cr}$  (N=56) are very close to the drip line and are prolate deformed. The  $\beta_2(n) - \beta_2(p)$  values for these nuclei show that the neutron deformation is larger than the corresponding proton deformation. This is just contrary to what has been seen for Cr nuclei near the proton drip line. In the case of the Cr isotopes, the protons and neutrons seem to play complementary roles at the proton and neutron drip lines, respectively, whereby deformations at both the drip lines are accentuated by the corresponding dripping nucleons. Thus, Cr nuclei present a unique example where nuclei on the proton drip line as well as on the neutron drip line are predicted to be more deformed than those about the stability line.

## 4.8 The Shape-coexistence

The phenomenon of shape coexistence is known to occur in several regions of the periodic table. Nuclei in the ground state assume two different deformations and two minima in the binding energy occur with a difference of a few hundred keV. Due to a complex potential-energy landscape in the deformation space, the associated shapes are usually of oblate and prolate types. The region of nuclei which we investigate in this work is prone to strong deformations on both the sides of the spherical shape. That the isotopes switch the shape from one type

of the deformation to another type on addition of a pair of neutrons is evident from Figs. 9 and 10. This effect is especially striking for Si and S chains whereby frequent shape changes are encountered in the minimum-energy state. Due to this softness of nuclei, it is expected that the two different shapes would coexist.

We show in Table 7 the nuclei which exhibit shape-coexistence in the RMF theory. The nuclei include an isotope each of Ne and Ar and several isotopes of Mg, Si and S. The difference in the binding energy of the prolate minimum and the oblate minimum is shown. A negative value implies that the prolate minimum lies lower than the corresponding oblate minimum. For all the Mg isotopes shown in the table the prolate shape is the lowest energy state with the oblate shape lying about 200-400 keV higher except for  $^{42}\text{Mg}$  where the difference exceeds 1 MeV. Thus, Mg isotopes  $^{26}\text{Mg}$ ,  $^{30}\text{Mg}$ ,  $^{44}\text{Mg}$  exhibit the shape-coexistence truly, wherein the nuclei possess considerable deformation of both the types.

Several Si isotopes are also shown to provide the occurrence of the shape coexistence. The nuclei  $^{26}\text{Si}$ ,  $^{30}\text{Si}$ ,  $^{38}\text{Si}$  and  $^{40}\text{Si}$  are predicted to be prolate deformed in the lowest energy state and are in coexistence with an oblate shape a few hundred keV above. Only for  $^{32}\text{Si}$ , the oblate shape is lowest in energy. The corresponding deformation for the shape-coexisting second minimum is very small so as to qualify it for a spherical shape. Thus, the oblate shape is in coexistence with the spherical one for  $^{32}\text{Si}$ .

The S isotopes which are predicted to show the shape coexistence are  $^{44}\text{S}$ ,  $^{48}\text{S}$ ,  $^{50}\text{S}$  and  $^{52}\text{S}$ . Except for  $^{48}\text{S}$ , S isotopes are oblate in the lowest energy state with a prolate shape within 200 keV of the lowest minimum. Here, the case of  $^{44}\text{S}$  is a celebrated one as this nucleus has the magic neutron number  $N=28$ . The shell effects associated to  $N=28$  are predicted to be quenched and the nucleus assumes a deformed shape. In its lowest energy state, the nucleus is oblate



( $\beta_2 = -0.19$ ). However, almost at about the same energy (within 30 keV), a highly deformed prolate shape ( $\beta_2 = 0.38$ ) coexists in its ground state. This is the largest deformation predicted for a sulphur isotope. It is singular to observe the almost degenerate two different shapes for this nucleus with the magic neutron number  $N=28$ .

## 4.9 The Isotope Shifts

We show in Fig. 13 the isotope shifts for nuclei in various isotopic chains. The isotope shifts have been obtained with respect to a reference nucleus (shown by a dark point) in each chain as given by

$$\delta r_c^2 = r_c^2 - r_c^2(ref) \quad (10)$$

It is interesting to note that the general behaviour of the isotope shifts as a function of isospin is similar for all the chains concerned here, i.e. the parabola like response is exhibited by all the isotopic chains. The minima in the isotope shifts correspond closely to nuclei near stability line and an upward trend in going to lighter nuclei implies that the nuclei with the minimum isotope shifts are smaller in charge radius even as compared to the lighter neighbours. The deformation of nuclei contributes partly to an increase in the size of the lighter isotopes. Such a phenomenon has been observed experimentally in general where nuclei are deformed [20]. Theoretically, the RMF theory was, for the first time ever, able to reproduce such a behaviour of the isotopes shifts, for example, in the isotopic chains of Sr and Kr nuclei [21] and for nuclei in the rare-earth region [19]. A similar behaviour is predicted here for the light nuclei. Experimental measurements on charge radii and isotope shifts are scanty and therefore a suitable comparison of our results with data is hindered.

For the highly neutron-deficient nuclei, the isotope shifts rise considerably above the zero level. A part of the rise to extreme left of each curve owes to the nuclei being close to the proton drip line whereby the charge radius swells due to a larger proton skin.

## 4.10 Deformation at Drip Lines

Drip lines are usually encountered near magic numbers. It was predicted in the RMF theory that the shell effects associated to the magic numbers near the neutron drip line are strong. This implies that a major gap in energy should exist for nuclei with particle number above the magic number. Consequently, nuclei near a major magic number tend to be spherical. Hence, it is widely expected that nuclei near a drip line should be spherical. However, in the present case, nuclei in this region are highly deformed and there are indications of quenching of the magic number  $N=28$ , thus, leading to strong deformations for nuclei possessing this neutron number. We have discussed deformation properties in Figs. 8 and 9 and in Tables 3-5. Here, we summarize deformed nuclei near drip lines.

It is interesting to observe from Figures 8 and 9 that the isotopes at the end of the chains of Ne, Mg, Si, Ar and Cr (except S and Ti) are deformed. These nuclei are all close to the neutron drip line and are also in the vicinity of  $N=28$ . Especially, Ne and Mg nuclei near the neutron drip line are highly prolate deformed ( $\beta_2 \sim 0.4$ ) whereas Si and Ar nuclei near the neutron drip line are predicted to be highly oblate in shape. For nuclei above  $Z=14$  (Si) the neutron drip line is encountered at neutron numbers well above  $N=28$ . As discussed in Section 4.6,  $^{44}\text{S}$  with  $N=28$  is predicted to be highly deformed, whereas S isotopes near neutron drip (above  $N=28$ ) show only a moderate deformation. Only for Ti, isotopes near neutron drip line are spherical as Ti lies in a traditionally spherical

domain of  $Z=20$ . However, Cr isotopes near neutron drip exhibit a reasonably strong deformation. It is noteworthy that these nuclei occur with a neutron number near  $N=50$  and yet lending themselves to a well deformed shape.

Here we have shown that the RMF theory predicts several instances of strong deformation near the neutron drip line. A comparison of the RMF with the FRDM results (Figs. 8 and 9) shows that for the case of Ne, Mg and Cr, both the RMF and FRDM predict strongly prolate shape for nuclei near the neutron drip line, whereas both predict strongly deformed oblate shape for Ar and Si nuclei in the vicinity of the neutron drip. The significant difference in the two predictions, however, appears for S isotopes near neutron drip. In the RMF, the S isotopes take up a spherical shape, whereas the FRDM predicts the corresponding nuclei to be strongly prolate deformed. The large positive value of  $\beta_2$  in the FRDM for  $^{54,56}\text{S}$  arises from an abrupt shape transition prolate-oblate-prolate at  $A=52$ . Such a behaviour is not noticed in the RMF predictions.

Examining the proton-rich side of the isotopic chains, we find that the RMF theory predicts well-deformed shapes also close to the proton drip line. For the Ne and Mg isotopes, the proton drip nuclei go down to  $N=8$  in the neutron number, thus forcing a spherical mean field. Thus, the nuclei  $^{18}\text{Ne}$  and  $^{20}\text{Mg}$  are predicted to be spherical. This is a reminder that  $N=8$  shell strength is maintained in the sd-shell nuclei. As the proton drip in Ne and Mg nuclei occurs very close to the stable nuclei, it is difficult to make an assessment of how the properties of nuclei change near the proton drip line. We examine other nuclear chains above  $Z=12$  for this purpose. For Si, the isotopes  $^{22}\text{Si}$  and  $^{24}\text{Si}$  are near the proton drip line. Here,  $^{22}\text{Si}$  is spherical due to  $N=8$ , which is already unbound and is therefore, not a truly drip line nucleus. However,  $^{24}\text{Si}$  has a proton Fermi energy of  $-1.66$  MeV. It is a proton drip nucleus and is significantly prolate deformed (see Fig.

8).

As we go to the S chain, we move away from the influence of  $N=8$  near the proton drip line. We obtain  $^{28}\text{S}$  ( $N=12$ ) as a proton drip nucleus with  $\lambda_p = -1.47$  MeV. It is noteworthy that this nucleus has a large prolate deformation ( $\beta_2 = 0.30$ ). This serves to illustrate the point that the mean field near the proton drip line can be substantially deformed.

Argon nuclei near the proton drip line show interesting features. The nuclei  $^{30}\text{Ar}$  and  $^{32}\text{Ar}$  are near the proton drip.  $^{30}\text{Ar}$  shows a well-deformed prolate shape ( $\beta_2 \sim 0.23$ ) in its ground state. However, at the same time there co-exists an oblate deformed ( $\beta_2 \sim -0.14$ ) minimum about 0.5 MeV above the prolate state. Thus, the shape coexistence seems to be preserved also near a drip line.  $^{32}\text{Ar}$  is also a proton drip nucleus, having an oblate deformation  $\beta_2 \sim -0.16$ . In contrast, Ti and Cr nuclei near proton drip are overwhelmingly spherical due to a strong influence from the magic number  $Z=20$ .

## 5 Summary and Conclusions

We have made an exhaustive study of the ground-state properties of nuclei in the light mass region. The study has covered complete isotopic chains encompassing nuclei near the stability line as well as those close to the neutron and proton drip lines. As nuclei in this region of the periodic table have significant deformation, we have employed an axially deformed basis to investigate the structure of nuclei in the RMF theory. We have used the force NL-SH which has been shown to describe the properties of nuclei all along the periodic table. The asymmetry energy plays an important role for nuclei far away from the stability line. In this respect, the force NL-SH which has a proper asymmetry energy has been shown to perform very well for nuclei with large isospins.

The ground-state binding energies and charge radii obtained in the RMF theory show a good agreement with the data where available. The neutron radii for very neutron-rich isotopes are found to exhibit an unusual increase as compared to their lighter counterparts. The increase in the neutron *rms* radius is more apparent above a major closed shell, thus reflecting the importance of the shell effects. Nuclei near the neutron drip line show signs of a neutron halo as the size of a nucleus swells significantly due to the last neutron orbitals being close to the continuum. However, the corresponding proton *rms* radius at the proton drip line does not increase as much due to the reason that the Coulomb repulsion brings about the proton drip with only a marginal difference in the neutron and proton number. Consequently, the proton halo in nuclei near the proton drip line is suppressed considerably as compared to a larger neutron halo expected near neutron drip line.

It is shown that nuclei in this region are strongly deformed. This deformation persists also for nuclei away from the stability line. Many nuclei near the drip lines are predicted to be strongly deformed. It is also predicted that the phenomenon of shape coexistence occurs in several nuclei in these isotopic chains. This is due to a complex evolution of the potential energy landscape in the deformation degrees of freedom of nuclei as a function of nuclear isospin. Such a feature is also exhibited by nuclei near the neutron drip line. Consequently, several isotopes of Mg, Si and S near the neutron drip line are shown to coexist in a well-deformed prolate and an oblate shape. The two states differ by a few keV in energy. In this respect, the nucleus  $^{44}\text{S}$  has shown a most remarkable character that two minimum-energy states of this nucleus, one a highly prolate and another well-deformed oblate, are almost degenerate in energy.

Examining the effect of the shell closures on deformation, it is shown that

major magic numbers such as 8, 20 and 50 respect the shell effects and lead to nuclei which are spherical. This effect is observable for nuclei about the stability line as well as near the drip lines. This shows that the major shell closures keep their magic nature even in going to the drip lines. In a broader sense, the shell effects near the drip lines are maintained as strong. This is in accord with our earlier assertion that the shell effects near the neutron drip line in medium-heavy nuclei remain strong [34].

The magic number  $N=28$ , however, exhibits different properties. For the isotopic chains below Ca, it is shown that the neutron number  $N=28$  loses its magic character and that the associated shell effects are washed out, implying that the shell gap at  $N=28$  is reduced significantly. Consequently, the corresponding nuclei deform strongly. The case of  $^{44}\text{S}$  is shown to be especially interesting as this nucleus with  $N=28$  assumes a strongly prolate and a strongly oblate shape which coexist in the ground state, as mentioned above.

We have employed the BCS pairing in the present study. For nuclei close to and not too far from the stability line, the BCS approach provides a reasonably good description of the pairing properties. However, in going to nuclei near the drip lines, coupling to continuum needs to be taken into account. Therefore, for such nuclei, the BCS pairing has limitations in that respect. The most appropriate framework for an improved prediction of such aspects is the relativistic Hartree-Bogoluebov approach in coordinate space. An application of the RHB approach for deformed nuclei has still not been accomplished and is work for future.

## 6 Acknowledgment

One of the authors (GAL) acknowledges support by the European Union under contract No. TMR-EU/ERB/FMBCICT-950216, by the Bundesministerium fuer Bildung und Forschung under the project 06 TM 743 (6) and by the Greek Secretariat of Research and Technology under contract PENED/1981.

## References

- [1] E. Roeckel, Rep. Prog. Phys. **55** (1992) 1661.
- [2] A. Mueller and B. Sherril, Ann. Rev. Nucl. Part. Sci. **43** (1993) 529.
- [3] I. Tanihata, Progr. Part. Nucl. Phys. **35** (1996) 435. (1995) 505.
- [4] J. Vervier, Progr. Part. Nucl. Phys. **37** (1996) 435.
- [5] Proc. 4th Int. Conf. on Radioactive Nuclear Beams, Omiya, Japan, Nucl. Phys. **A616** (1997).
- [6] D. Vautherin, Phys. Rev. **C7** (1973) 296.
- [7] P. Quentin and H. Flocard, Ann. Rev. Nucl. Sci. **28** (1978) 523.
- [8] J. Decharge, M. Girod, and D. Gogny, Phys. Lett. **55B** (1975) 361.
- [9] J. Decharge and D. Gogny, Phys. Rev. **C 21** (1980) 1568.
- [10] B.D. Serot and J.D. Walecka, Adv. Nucl. Phys. **16** (1986) 1.
- [11] P.G. Reinhard, Rep. Prog. Phys. **52** (1989) 439.
- [12] B.D. Serot, Rep. Prog. Phys. **55** (1992) 1855.
- [13] P. Ring, Progr. Part. Nucl. Phys. **37** (1996) 193.
- [14] N. Tajima, P. Bonche, H. Flocard, P.-H. Heenen, and M.S. Weiss, Nucl. Phys. **A551** (1993) 434.
- [15] M.M. Sharma, G.A. Lalazissis, and P. Ring, Phys. Lett. **B317** (1993) 9.
- [16] G.A. Lalazissis, M.M. Sharma, J. König and P. Ring, in Proc. of Inter. Conf. on Nuclear Shapes and Nuclear Structure at Low Excitation Energies, Antibes (France), (eds.) M. Vergnes, D. Goutte, P.H. Heenen and J. Sauvage, Editions Frontieres, (1994) p. 161.
- [17] M.M. Sharma, G.A. Lalazissis, J. König, and P. Ring, Phys. Rev. Lett. **74** (1995) 3744.

- [18] P.-G. Reinhard and H. Flocard, Nucl. Phys. **A584** (1995) 467.
- [19] G.A. Lalazissis, M.M. Sharma and P. Ring, Nucl. Phys. **A597** (1996) 35.
- [20] E.W. Otten, in *Treatise on Heavy-Ion Science*, edited by D.A. Bromley (Plenum, New York, 1989) Vol 7, p. 515.
- [21] G.A. Lalazissis and M.M. Sharma, Nucl. Phys. **A586** (1995) 201.
- [22] P. Bonche, J. Dobaczewski, H. Flocard and P.H. Heenen, Nucl. Phys. **A530** (1991) 149.
- [23] P.H. Heenen, P. Bonche, J. Dobaczewski and H. Flocard Nucl. Phys. **A561** (1993) 367.
- [24] T.R. Werner, J.A. Sheikh, W. Nazarewicz, M.R. Strayer, A.S. Umar and M. Misu, Phys. Lett. **B 333** (1994) 303.
- [25] T.R. Werner, J.A. Sheikh, M. Misu W. Nazarewicz, J. Rikowska, K. Heeger, A.S. Umar and M.R. Strayer, Nucl. Phys. **A597** (1996) 327.
- [26] Z. Ren, W. Mittig, B. Chen, Z. Ma and G. Auger, Z. Phys. **A353** (1996) 363.
- [27] J.P. Maharana, L.S. Warriar and Y.K. Gambhir, Ann. Phys. (N.Y.) **250** (1996) 237.
- [28] F. Grümmer, B.Q. Chen, Z.Y. Ma and S. Krewald, Phys. Lett. **B387** (1996) 673.
- [29] K.L. Kratz, Rev. Mod. Astron. **1** (1988) 184.
- [30] K.L. Kratz, J.P. Bitouzet, F.K. Thielemann, P. Möller and B. Pfeiffer, Astrophys. J **403** (1993) 216.
- [31] P. Haustein, At. Data Nucl. Data Tables, **39** (1988) 185.
- [32] P. Möller, J.R. Nix, W.D. Myers, and W.J. Swiatecki, Atomic Data and Nuclear Data Tables **59** (1995) 185.
- [33] Y. Aboussir, J.M. Pearson, A.K. Dutta, and F. Tondeur, Atomic Data and Nuclear Data Tables **61** (1995) 127.
- [34] M.M. Sharma, G.A. Lalazissis, W. Hillebrandt, and P. Ring, Phys. Rev. Lett. **72** (1994) 1431.
- [35] M.M. Sharma, G.A. Lalazissis, W. Hillebrandt, and P. Ring, Phys. Rev. Lett. **73** (1994) 1870.
- [36] J. Meng and P. Ring, Phys. Rev. Lett. (in press).
- [37] J. Boguta and A.R. Bodmer, Nucl. Phys. **A292** (1977) 413.
- [38] R.J. Furnstahl, B.D. Serot and H.B. Tang, Nucl. Phys. **A598** (1996) 539.



- [39] Y.K. Gambhir, P. Ring, and A. Thimet, *Ann. Phys. (N.Y.)* **198** (1990) 132.
- [40] P. Möller and J.R. Nix, *Nucl. Phys.* **A536** (1992) 20.
- [41] M.M. Sharma, M.A. Nagarajan, and P. Ring, *Phys. Lett.* **B312** (1993) 377.
- [42] G. Audi and A.H. Wapstra, *Nucl. Phys.* **A565** (1993) 1.
- [43] F. Buchinger, E.B. Ramsay, E. Arnold, W. Neu, R. Neugart, K. Wendt, R.R. Sivermans, P. Lievens, L. Vermeeren, D. Berdichevsky, R. Fleming, D.W.L. Sprung and G. Ulm, *Phys. Rev.* **C41** (1990) 2883.
- [44] M. Keim, E. Arnold, W. Borchers, U. Georg, A. Klein, R. Neugart, L. Vermeeren, R.R. Sivermans, P. Lievens and the ISOLDE Collaboration, *Nucl. Phys.* **A586** (1995) 219.
- [45] H. de Vries, C.W. De Jager and C. de Vries, *At. Data Nucl. Data Tables* **36** (1987) 495.
- [46] S. Raman, C.H. Malarkey, W.T. Milner, C.W. Nestor and P.H. Stelson, *At. Data Nucl. Data Tables* **36** (1987) 1.
- [47] H. Scheit et al, *Phys. Rev. Lett.* **77** (1996) 3967.
- [48] O. Sorlin et al., *Phys. Rev. C* **47** (1993) 2941.

## Figure Captions

- Fig. 1** The charge ( $r_c$ ) and neutron ( $r_n$ ) *rms* radii of nuclei obtained in the deformed RMF calculations using the force NL-SH. The charge radius has been obtained by folding the finite proton size on to the proton *rms* radius. A few experimental charge radii available and some results from the predictions of ETF-SI as available are also shown for comparison.
- Fig. 2** The same as in Fig. 1, for other isotopic chains.
- Fig. 3** The neutron skin thickness (proton skin thickness, respectively) ( $r_n - r_p$ ) for neutron-rich and proton-rich nuclei in various isotopic chains. The effect of the Coulomb force in expanding the proton *rms* radius rapidly can be visualized in a stronger slope of the curve for proton-rich nuclei.
- Fig. 4** The L=0 component of the neutron and proton vector (baryonic) densities for a few nuclei near the neutron drip line. A staggeringly large neutron halo and a higher neutron density in the interior as compared to protons is present.
- Fig. 5** The same as in Fig. 4 for nuclei near proton drip. The proton skin thickness and the formation of a proton halo is subdued due to the Coulomb barrier.
- Fig. 6** The 2-neutron separation energy in the RMF theory.
- Fig. 7** The 2-proton separation energy in the RMF theory.
- Fig. 8** The quadrupole deformation ( $\beta_2$ ) in the RMF theory. A comparison is made with the results from FRDM and ETF-SI where available.
- Fig. 9** The same as in Fig. 8 for other isotopic chains.
- Fig. 10** The difference in the quadrupole deformations of the neutron and proton mean-fields in the RMF theory.
- Fig. 11** The same as in Fig. 10 for other isotopic chains.
- Fig. 12** The isotope shifts obtained in the RMF theory for various isotopic chains. The reference nucleus chosen for each chain for calculating the difference is shown by dark points.

Table 1: The binding energies (in MeV) for even-even Ne and Mg Si and S isotopes obtained with the force NL-SH. The predictions from the mass models FRDM and ETF-SI (wherever available) are also shown for comparison. The empirical values (expt.) available are also shown.

Ne Nuclei					Mg Nuclei				
A	RMF	FRDM	ETF-SI	expt.	A	RMF	FRDM	ETF-SI	expt
18	134.10	134.25	-	132.14	20	135.90	135.97	-	134.35
20	155.38	161.32	-	160.64	22	166.65	169.68	-	168.57
22	175.96	178.44	-	177.77	24	194.34	198.40	-	198.26
24	190.12	191.87	-	191.84	26	213.34	216.86	-	216.68
26	200.66	201.01	-	201.60	28	229.01	231.11	-	231.63
28	208.71	208.15	-	206.89	30	240.43	241.89	-	241.63
30	215.57	211.88	-	212.08	32	251.03	250.32	-	249.69
32	216.47	217.14	-	213.28	34	256.28	257.15	-	256.59
34	218.80	217.04	-	-	36	262.90	262.02	259.38	260.27
36	218.47	213.97	207.35	-	38	265.93	264.58	260.92	-
38	215.59	214.04	-	-	40	267.28	268.05	-	-
					42	267.71	264.09	-	-
					44	266.45	267.69	-	-

Si Nuclei					S Nuclei				
A	RMF	FRDM	ETF-SI	expt.	A	RMF	FRDM	ETF-SI	expt
22	136.00	133.45	-	134.45	26	169.69	169.60	-	171.37
24	170.19	172.94	-	172.00	28	206.74	209.60	-	209.41
26	202.70	207.25	-	206.05	30	239.32	241.92	-	243.69
28	231.99	236.15	-	236.54	32	265.84	269.52	-	271.78
30	251.00	253.67	-	255.62	34	286.12	290.23	-	291.84
32	268.24	269.63	-	271.41	36	305.75	308.00	308.15	308.71
34	283.69	282.98	-	283.43	38	318.61	321.97	321.19	321.05
36	292.13	292.99	291.82	292.02	40	332.51	334.22	333.14	333.18
38	300.16	301.49	299.76	299.50	42	343.55	344.27	343.08	343.72
40	306.36	307.08	305.80	306.50	44	350.03	352.00	351.52	353.50
42	312.74	315.17	311.54	-	46	356.51	357.05	357.27	-
44	315.68	315.02	313.59	-	48	360.63	360.86	361.61	-
46	317.28	318.05	315.03	-	50	363.97	363.40	363.55	-
					52	366.32	362.71	360.89	-
					54	368.02	362.60	-	-
					56	369.60	361.86	-	-

Table 2: The binding energies of Ti, Cr and Ar isotopes. Refer to the caption of Table 1 for details.

Ti Nuclei					Cr Nuclei				
A	RMF	FRDM	ETF-SI	expt.	A	RMF	FRDM	ETF-SI	expt
34	194.33	193.77	-	-	38	231.72	232.29	-	-
36	239.18	239.83	-	240.66	40	275.10	275.68	277.58	-
38	276.90	280.29	280.80	280.40	42	312.33	314.78	317.99	314.23
40	312.52	316.04	315.84	314.49	44	348.94	351.02	351.26	349.90
42	346.15	348.69	347.17	346.91	46	378.63	382.63	381.81	381.98
44	370.97	376.76	373.23	375.47	48	408.15	411.16	409.65	411.46
46	394.39	399.17	397.07	398.19	50	432.84	435.39	433.99	435.04
48	416.00	420.10	418.21	418.70	52	454.74	457.29	455.64	456.35
50	436.64	438.66	437.26	437.78	54	471.34	474.55	474.08	474.00
52	449.06	452.72	452.40	451.96	56	485.55	489.02	489.32	488.51
54	460.09	464.17	465.24	464.25	58	498.23	501.84	501.86	501.25
56	470.40	474.37	474.89	473.91	60	509.35	513.42	512.51	512.33
58	480.17	483.05	482.33	-	62	520.38	522.83	522.15	-
60	489.90	491.02	488.77	-	64	531.42	532.74	530.79	-
62	498.96	497.89	494.21	-	66	538.61	540.26	538.13	-
64	503.63	503.43	498.86	-	68	546.82	547.42	544.38	-
66	506.73	507.75	502.70	-	70	553.15	553.58	549.82	-
68	510.98	511.23	505.74	-	72	557.32	558.23	554.06	-
70	513.26	514.13	507.78	-	74	559.78	562.49	557.31	-
72	514.59	516.46	509.03	-	76	561.94	563.44	558.85	-
74	515.92	515.64	508.97	-	78	563.34	563.50	559.69	-
					80	563.75	561.79		-

Ar Nuclei					
A	RMF	FRDM	ETF-SI	expt.	
28	165.64	166.11	-	-	
30	205.96	208.11	-	207.97	
32	243.61	246.32	-	246.38	
34	273.29	277.37	-	278.72	
36	302.83	306.05	304.19	306.72	
38	324.39	328.01	326.23	327.34	
40	341.42	345.30	343.77	343.81	
42	357.27	360.53	359.62	359.34	
44	372.15	374.36	373.46	373.32	
46	385.62	386.19	386.00	386.92	
48	393.44	394.58	394.94	396.56	
50	400.16	400.96	401.99	-	
52	406.33	405.92	406.33	-	
54	410.81	408.91	407.07	-	
56	414.70	412.93	407.21	-	
58	418.60	413.57	-	-	
60	418.80	414.64	-	-	

Table 3: The  $\beta_2$  and  $\beta_4$  deformation parameters calculated in the RMF theory with the NL-SH force for various even-even Ne ( $Z=10$ ) Mg ( $Z=12$ ) and Si ( $Z=14$ ) isotopes. Predictions from the mass models FRDM and ETF-SI are also shown for comparison. For the values given in the parenthesis, refer to the text.

Z	A	N	$\beta_2$			$\beta_4$		
			RMF	FRDM	ETF-SI	RMF	FRDM	ETF-SI
10	18	8	0.002	0.109	-	0.000	0.150	-
	20	10	0.241	0.335	-	0.059	0.428	-
	22	12	0.408	0.326	-	0.065	0.225	-
	24	14	0.178 (-0.107)	-0.215	-	0.021	0.155	-
	26	16	0.002	0.000	0.370	0.000	-0.014	0.000
	28	18	0.001	-0.204	-	0.000	-0.127	-
	30	20	0.000	0.000	-	0.000	-0.014	-
	32	22	0.004	0.238	-	0.000	0.281	-
	34	24	0.377	0.308	-	0.194	0.220	-
	36	26	0.430	0.309	-	0.079	0.065	-
	38	28	0.443	-0.292	-	-0.088	0.196	-
12	20	8	0.000	0.147	-	0.001	-0.091	-
	22	10	0.426	0.326	-	0.080	0.225	-
	24	12	0.465 (-0.204)	0.374	-	0.005	-0.053	-
	26	14	0.298 (-0.219)	-0.310	-	0.000	0.186	-
	28	16	0.288 (-0.164)	0.323	-	-0.027	-0.136	-
	30	18	0.189 (-0.134)	-0.222	-	-0.017	-0.112	-
	32	20	0.000	0.000	-	0.000	0.000	-
	34	22	0.173	0.406	-	0.042	0.062	-
	36	24	0.383 (-0.165)	0.328	0.350	0.071	0.085	0.070
	38	26	0.413 (-0.246)	0.314	0.390	0.020	-0.037	-0.010
	40	28	0.449 (-0.354)	-0.290	-	-0.086	0.211	-
	42	30	0.414 (-0.300)	0.265	-	-0.056	-0.015	-
	44	32	0.317 (-0.243)	0.175	-	-0.049	-0.317	-
14	22	8	0.000	0.000	-	0.000	0.000	-
	24	10	0.240 (-0.140)	-0.242	-	0.037	0.202	-
	26	12	0.330 (-0.230)	-0.353	-	-0.002	0.226	-
	28	14	-0.287	-0.478	-	0.070	0.250	-
	30	16	-0.185 (0.122)	0.000	-	0.007	0.000	-
	32	18	0.028 (-0.151)	0.000	-	0.004	0.000	-
	34	20	0.000	0.000	-	0.000	0.000	-
	36	22	0.000	0.000	0.180	0.000	0.000	0.050
	38	24	0.248 (-0.155)	0.234	0.260	0.048	0.094	0.050
	40	26	0.291 (-0.240)	-0.592	-0.310	0.002	0.143	0.040
	42	28	-0.342 (0.425)	-0.321	-0.350	0.164	0.218	0.050
	44	30	-0.304 (0.137)	-0.263	-0.300	0.083	0.071	-0.030
	46	32	-0.255	0.023	-0.180	0.013	-0.291	-0.070

Table 4: As in Table but for S (Z=16) and Ar (Z=18) isotopes.

Z	A	N	$\beta_2$			$\beta_4$		
			RMF	FRDM	ETF-SI	RMF	FRDM	ETF-SI
16	26	10	0.004	0.000	-	0.000	0.000	-
	28	12	0.307	0.346	-	-0.011	-0.159	-
	30	14	-0.200	0.000	-	0.016	0.000	-
	32	16	0.235	0.000	-	-0.042	0.000	-
	34	18	0.146	0.000	-	-0.023	0.000	-
	36	20	0.000	0.000	0.020	0.000	0.000	-0.030
	38	22	-0.043	0.000	0.160	0.001	0.000	0.010
	40	24	0.242	0.254	0.260	0.008	-0.001	0.020
	42	26	0.259	0.249	0.250	-0.027	-0.076	-0.020
	44	28	-0.195 (0.375)	0.000	-0.260	0.047	-0.008	0.030
	46	30	0.209	0.219	-0.250	-0.064	-0.048	-0.050
	48	32	0.201 (-0.203)	0.241	-0.180	-0.029	-0.086	-0.070
	50	34	-0.218 (0.169)	0.255	0.010	-0.038	-0.139	0.000
	52	36	-0.168 (0.130)	-0.406	-0.130	-0.038	-0.035	0.030
	54	38	0.078 (-0.087)	0.434	-	-0.019	-0.051	-
56	40	0.000	0.461	-	0.000	-0.102	-	
18	28	10	0.000	-0.243	-	0.000	-0.244	-
	30	12	0.226 (-0.138)	-0.251	-	-0.019	-0.168	-
	32	14	-0.159	-0.272	-	-0.013	-0.114	-
	34	16	0.163	0.000	-	-0.025	0.000	-
	36	18	-0.195	0.000	-0.240	-0.057	0.000	-0.060
	38	20	0.000	0.000	0.000	0.000	0.000	-0.010
	40	22	0.000	0.000	0.140	0.000	0.000	0.000
	42	24	0.122	0.000	0.180	0.001	0.000	0.010
	44	26	0.122	0.000	0.190	0.010	0.000	0.000
	46	28	0.000	0.000	-0.230	0.000	0.000	0.030
	48	30	-0.138	-0.207	-0.250	-0.009	-0.067	-0.050
	50	32	-0.196 (0.088)	-0.248	-0.180	-0.024	-0.089	-0.070
	52	34	-0.224 (0.095)	-0.306	0.010	-0.039	-0.105	0.000
	54	36	-0.186 (0.066)	-0.357	-0.170	-0.051	-0.056	-0.040
	56	38	-0.100	-0.237	-0.160	-0.027	-0.126	-0.050
58	40	0.001	-0.255	-	0.000	-0.123	-	
60	42	0.000	-0.285	-	0.000	-0.161	-	

Table 5: As in Table but for Ti (Z=22) and Cr (Z=24) isotopes.

Z	A	N	$\beta_2$			$\beta_4$		
			RMF	FRDM	ETF-SI	RMF	FRDM	ETF-SI
22	34	12	0.206	0.444	-	0.051	0.074	-
	36	14	0.000	0.000	0.220	0.000	0.000	0.060
	38	16	-0.050	0.000	0.160	0.001	0.000	0.010
	40	18	0.000	0.000	0.140	0.000	0.000	0.020
	42	20	0.000	0.000	0.000	0.000	0.000	-0.010
	44	22	0.000	0.000	0.160	0.000	0.000	0.050
	46	24	0.112	0.000	0.220	0.027	0.000	0.060
	48	26	0.000	0.000	0.170	0.000	0.000	0.020
	50	28	0.000	0.000	0.080	0.000	0.000	0.010
	52	30	0.000	0.000	0.140	0.000	0.000	0.000
	54	32	0.120	0.000	0.020	0.012	0.000	0.000
	56	34	0.122	0.135	0.020	-0.006	-0.018	0.000
	58	36	-0.089	-0.105	0.070	-0.005	-0.011	-0.010
	60	38	-0.001	-0.079	0.060	0.000	-0.029	0.000
	62	40	0.000	0.000	0.020	0.000	0.000	0.000
	64	42	0.000	0.027	0.230	0.000	0.000	0.050
	66	44	0.001	0.147	0.200	0.000	0.108	0.050
68	46	0.146	0.152	0.190	0.048	0.067	0.040	
70	48	0.112	0.099	0.170	0.020	-0.021	0.000	
72	50	0.000	0.045	-0.090	0.000	0.001	0.030	
74	52	0.007	0.119	-0.130	0.000	0.105	0.030	
24	38	14	0.287	0.234	-	0.061	0.139	-
	40	16	0.262	0.273	0.300	0.014	0.027	0.040
	42	18	0.124	0.000	0.240	0.003	0.000	0.030
	44	20	0.000	0.000	0.150	0.000	0.000	0.030
	46	22	0.114	0.000	0.240	0.030	0.000	0.060
	48	24	0.248	0.000	0.260	0.072	0.000	0.070
	50	26	0.204	0.000	0.240	0.025	0.000	0.030
	52	28	0.000	0.000	0.140	0.000	0.000	0.020
	54	30	0.177	0.180	0.180	0.034	0.045	0.000
	56	32	0.212	0.189	0.130	0.015	0.022	0.010
	58	34	0.204	0.199	0.150	-0.020	-0.026	0.000
	60	36	0.153	0.181	0.170	-0.021	-0.021	0.020
	62	38	-0.047	0.329	0.280	-0.005	0.047	0.060
	64	40	0.000	0.018	0.280	0.000	0.000	0.060
	66	42	0.000	0.053	0.270	0.000	0.009	0.050
	68	44	0.179	0.161	0.260	0.069	0.084	0.040
	70	46	0.200	0.169	0.210	0.054	0.062	0.040
72	48	0.188	0.126	0.180	0.028	-0.019	0.010	
74	50	0.002	0.053	0.020	0.000	0.001	0.000	
76	52	0.036	0.142	0.140	0.003	0.091	0.020	
78	54	0.149	0.178	0.130	0.020	0.072	-0.020	
80	56	0.162	0.254	-	0.003	0.152	-	

Table 6: The quadrupole deformations  $\beta_2$  for various nuclei in the RMF theory. The available empirical deformations (expt.) obtained from BE(2) values [46] are also given. The experimental values for a few S (A=38-42) and Ar (A=44,46) isotopes are taken from the recent measurements [47]. The experimental values do not show the sign of the deformation.

Nucleus	RMF	expt.	Nucleus	RMF	expt.
<sup>18</sup> Ne	0.002	0.691	<sup>42</sup> S	0.259	0.300
<sup>20</sup> Ne	0.241	0.728	<sup>34</sup> Ar	0.162	0.238
<sup>22</sup> Ne	0.408	0.562	<sup>36</sup> Ar	-0.195	0.273
<sup>24</sup> Ne	0.178	0.410	<sup>38</sup> Ar	0.000	0.162
<sup>22</sup> Mg	0.432	0.560	<sup>40</sup> Ar	0.000	0.251
<sup>24</sup> Mg	0.465	0.606	<sup>42</sup> Ar	0.122	0.273
<sup>26</sup> Mg	0.298	0.482	<sup>44</sup> Ar	0.122	0.241
<sup>28</sup> Mg	0.288	0.485	<sup>46</sup> Ar	0.000	0.176
<sup>26</sup> Si	0.329	0.444	<sup>42</sup> Ti	0.000	0.310
<sup>28</sup> Si	-0.287	0.407	<sup>44</sup> Ti	0.000	0.262
<sup>30</sup> Si	-0.185	0.316	<sup>46</sup> Ti	0.112	0.317
<sup>32</sup> Si	0.028	0.345	<sup>48</sup> Ti	0.000	0.269
<sup>30</sup> S	-0.200	0.336	<sup>50</sup> Ti	0.000	0.166
<sup>32</sup> S	0.235	0.312	<sup>48</sup> Cr	0.248	0.335
<sup>34</sup> S	0.146	0.252	<sup>50</sup> Cr	0.204	0.293
<sup>36</sup> S	0.000	0.164	<sup>52</sup> Cr	0.000	0.224
<sup>38</sup> S	-0.043	0.246	<sup>54</sup> Cr	0.177	0.250
<sup>40</sup> S	0.242	0.284			



Table 7: Nuclei with a shape coexistence in the ground state. The difference in the energy of the ground state in the prolate and oblate shape is given. The associated deformations are also shown.

Nucleus	$E_{pro} - E_{obl}$	$\beta_2(pro.)$	$\beta_2(obl.)$
$^{24}\text{Ne}$	-0.170	0.177	-0.107
$^{26}\text{Mg}$	-0.370	0.300	-0.219
$^{30}\text{Mg}$	-0.406	0.190	-0.133
$^{42}\text{Mg}$	-1.374	0.410	-0.300
$^{44}\text{Mg}$	-0.236	0.320	-0.240
$^{26}\text{Si}$	-0.232	0.330	-0.230
$^{30}\text{Si}$	-0.110	0.120	-0.185
$^{32}\text{Si}$	0.455	0.030	-0.150
$^{38}\text{Si}$	-0.790	0.250	-0.155
$^{40}\text{Si}$	-0.170	0.290	-0.240
$^{44}\text{S}$	0.030	0.375	-0.190
$^{48}\text{S}$	-0.160	0.200	-0.200
$^{50}\text{S}$	0.208	0.170	-0.220
$^{52}\text{S}$	0.145	0.130	-0.170
$^{54}\text{S}$	0.026	0.078	-0.087
$^{30}\text{Ar}$	-0.650	0.230	-0.140

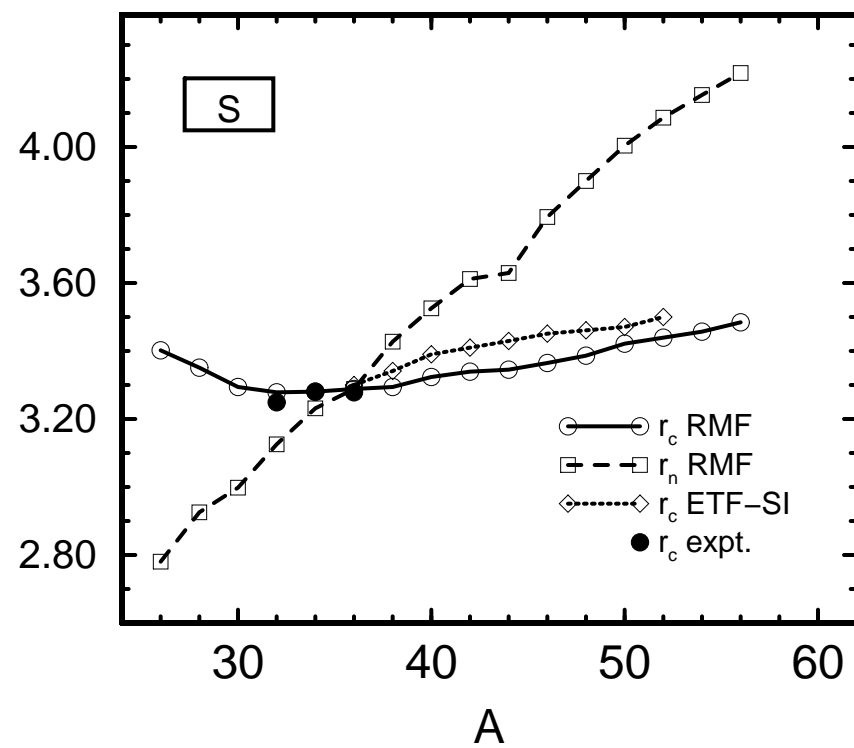
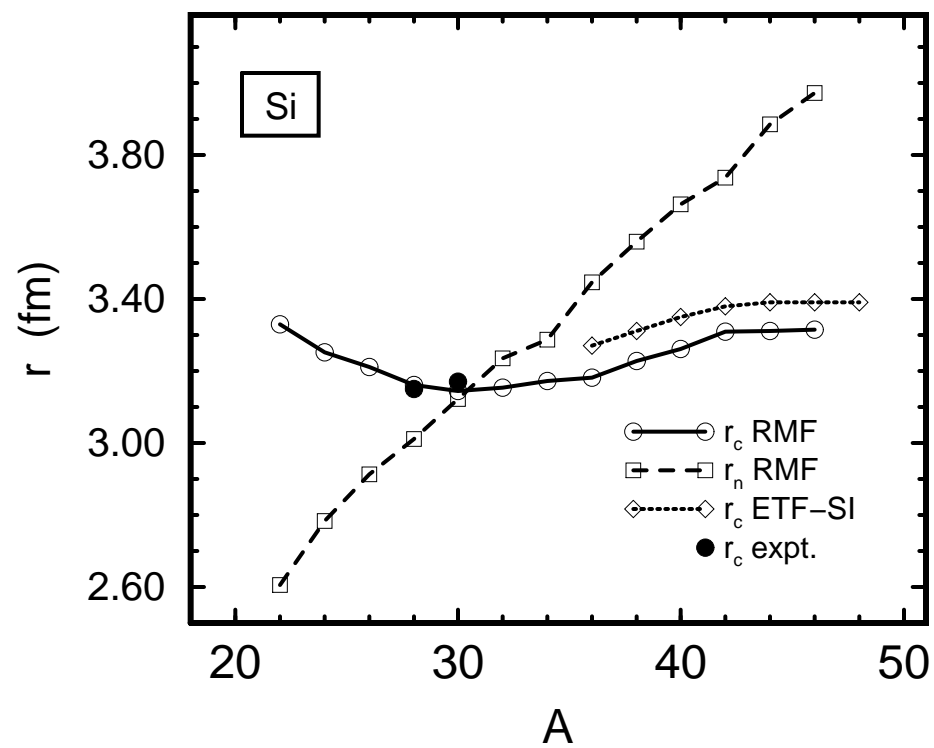
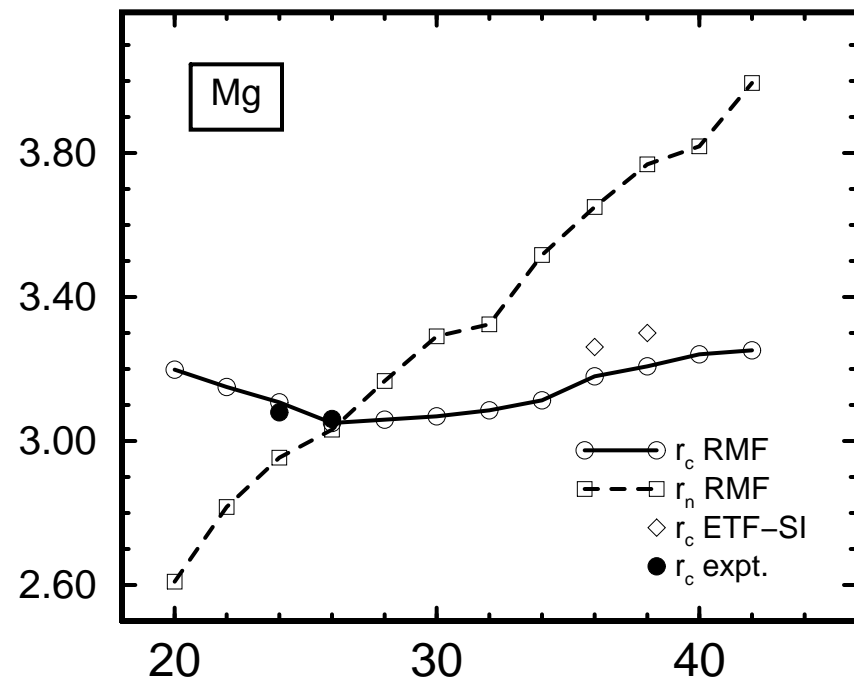
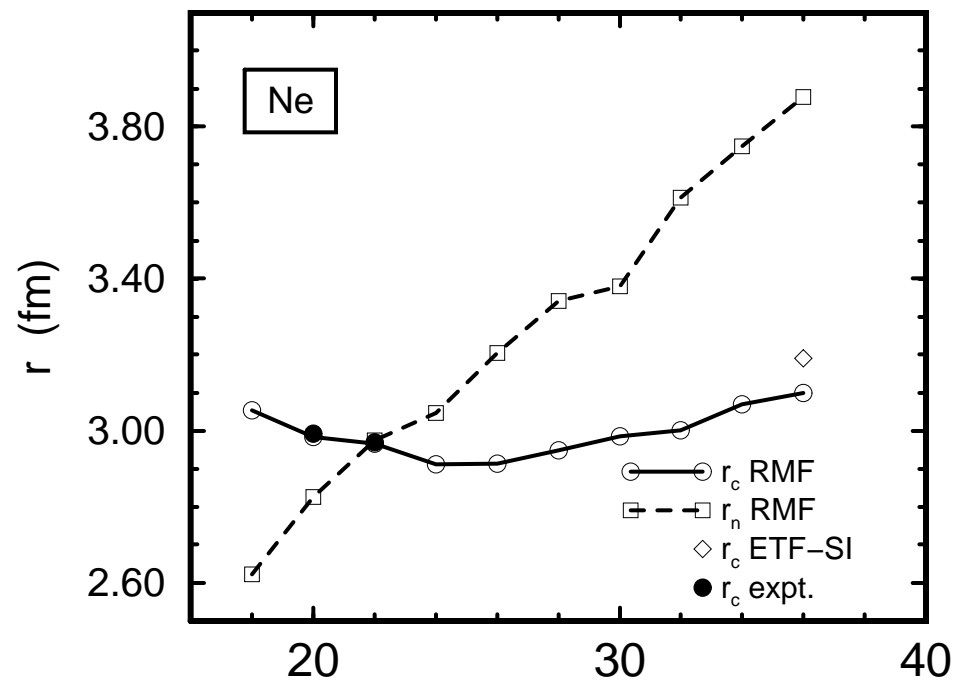


Fig. 1

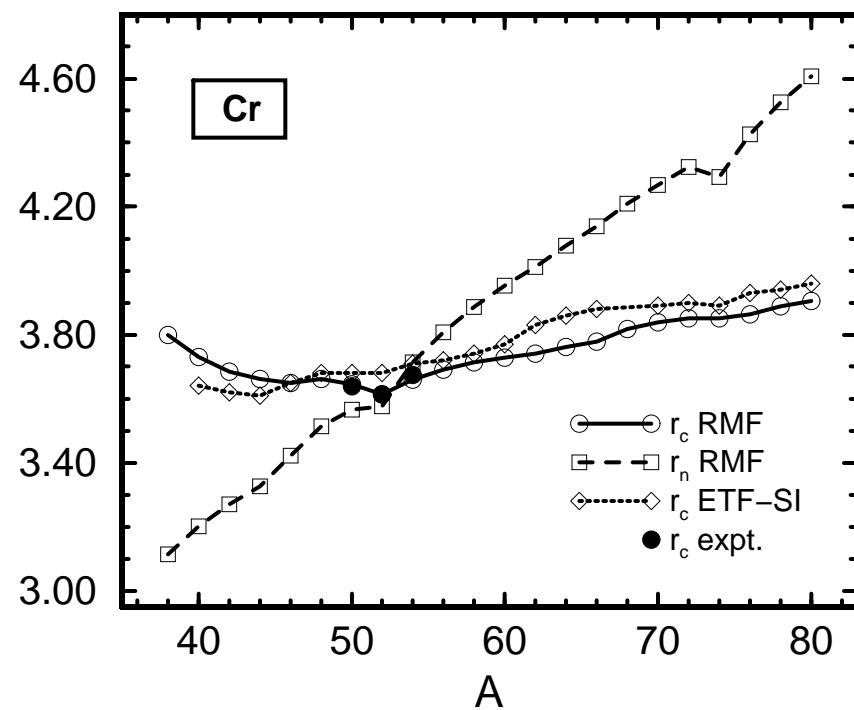
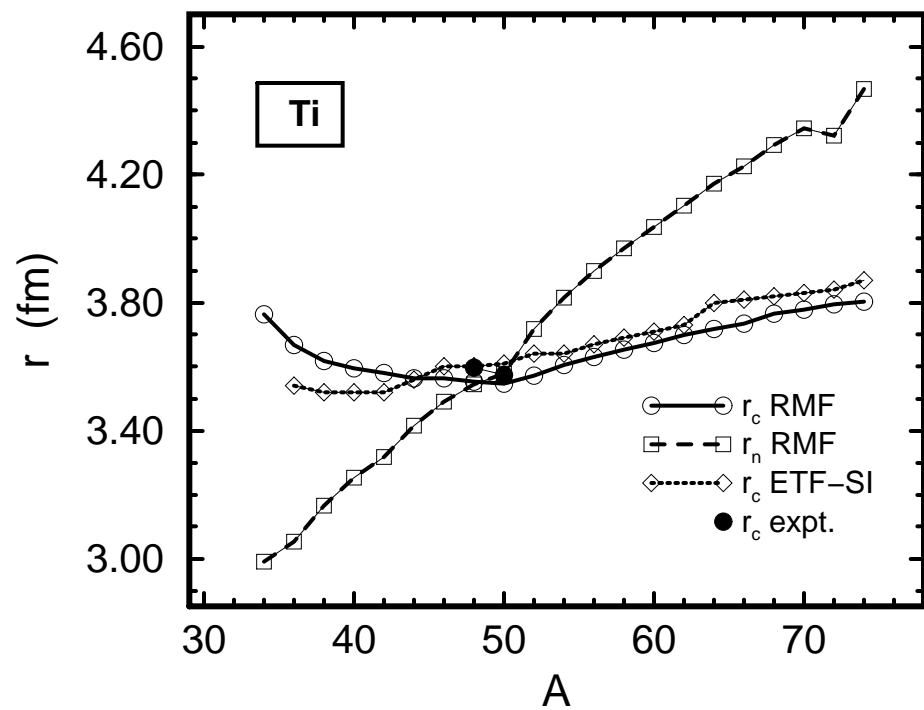
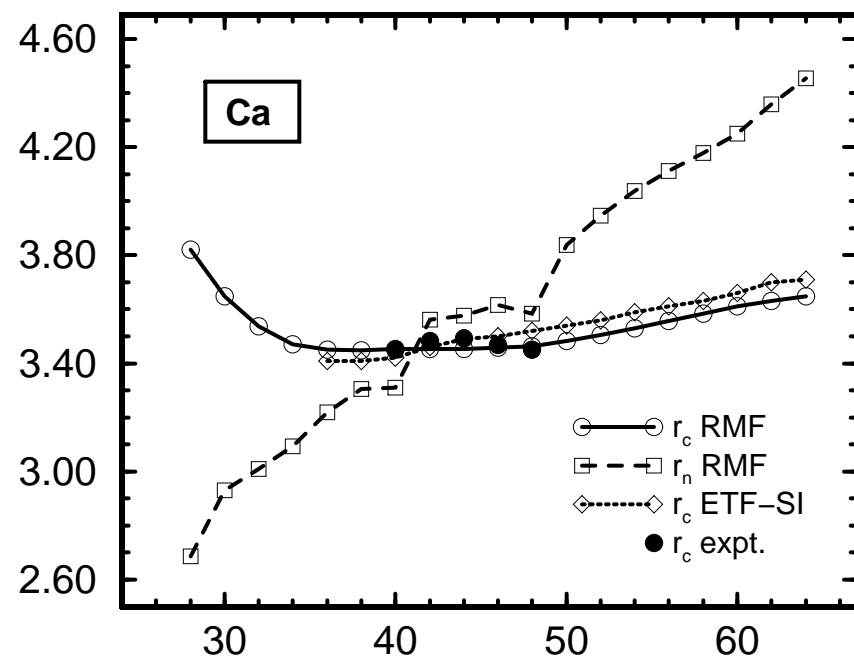
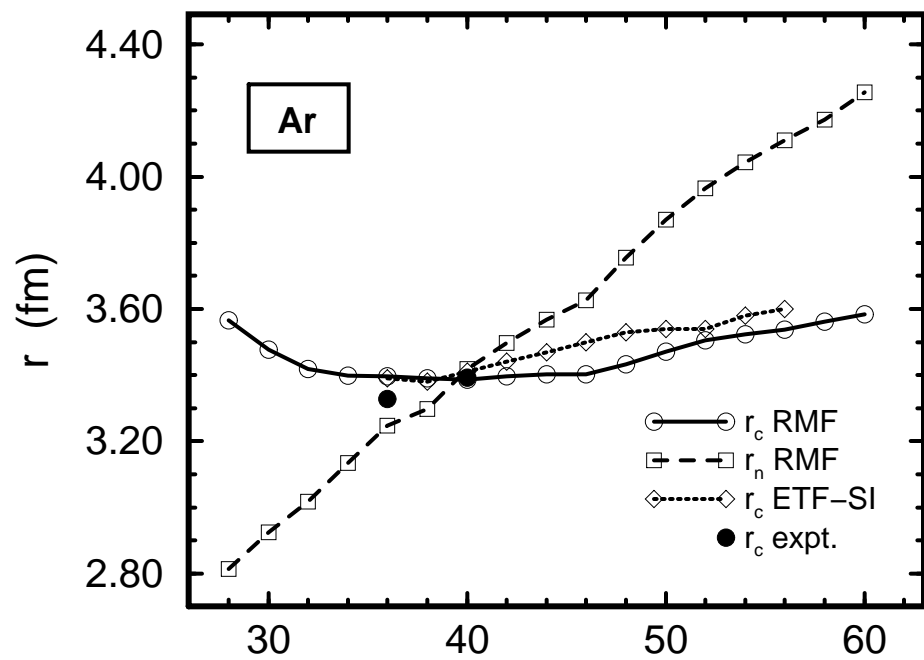
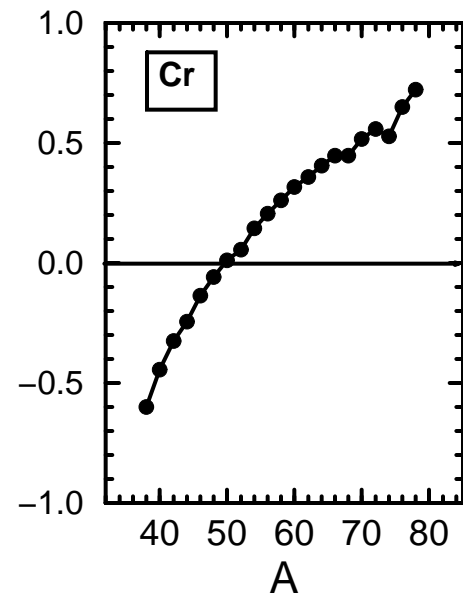
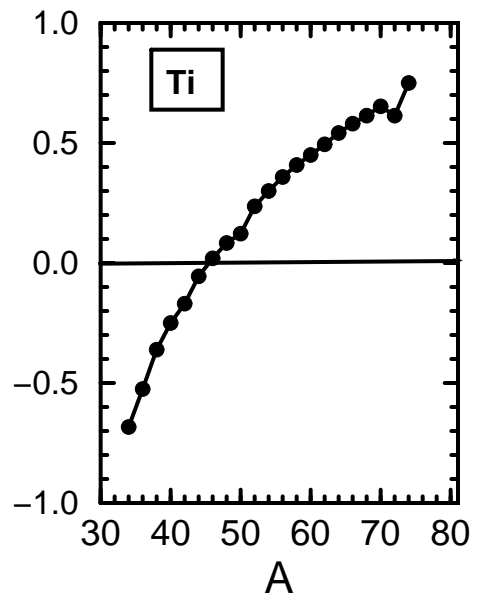
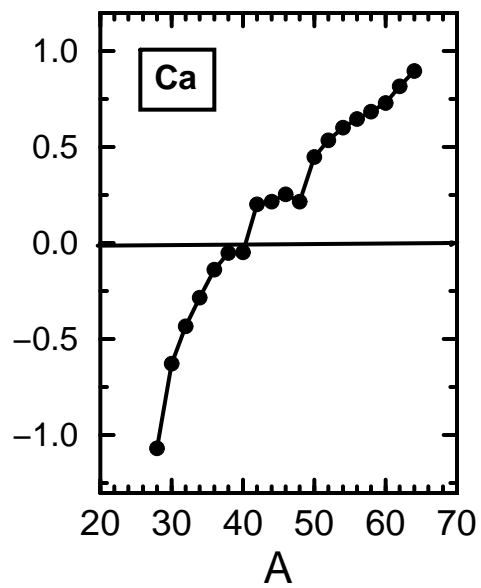
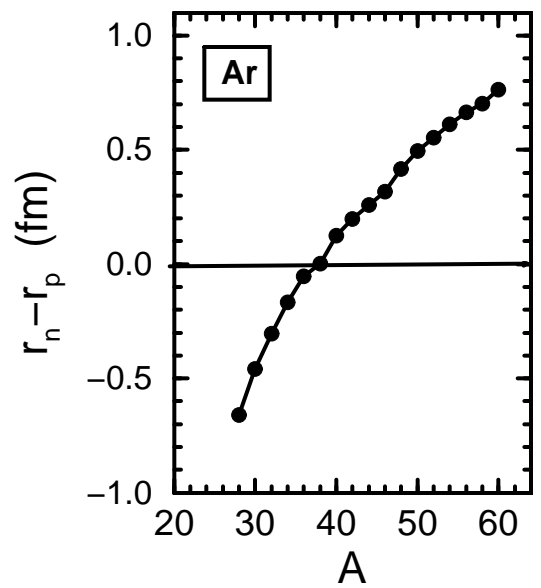
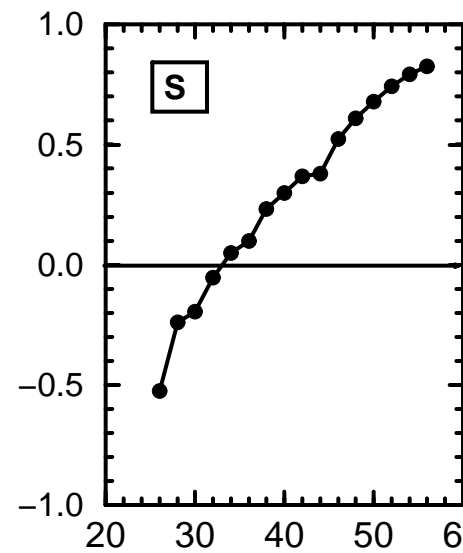
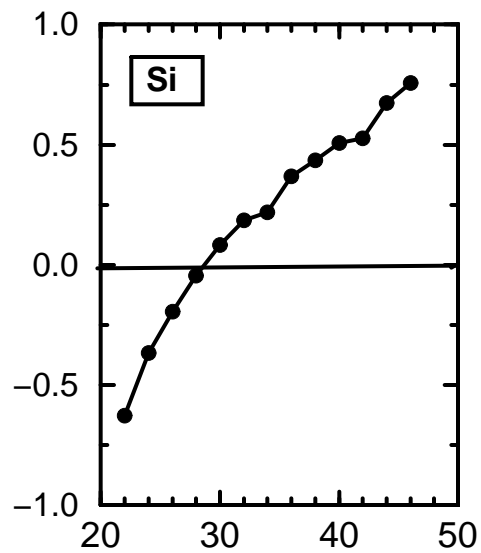
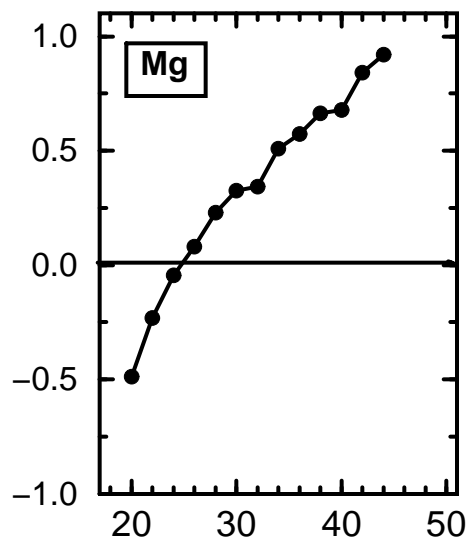
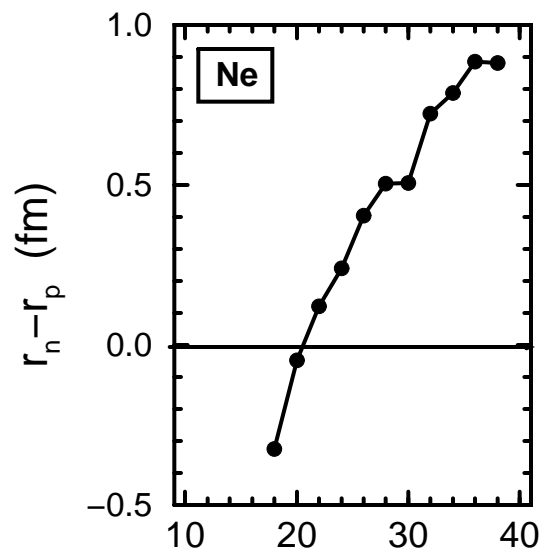
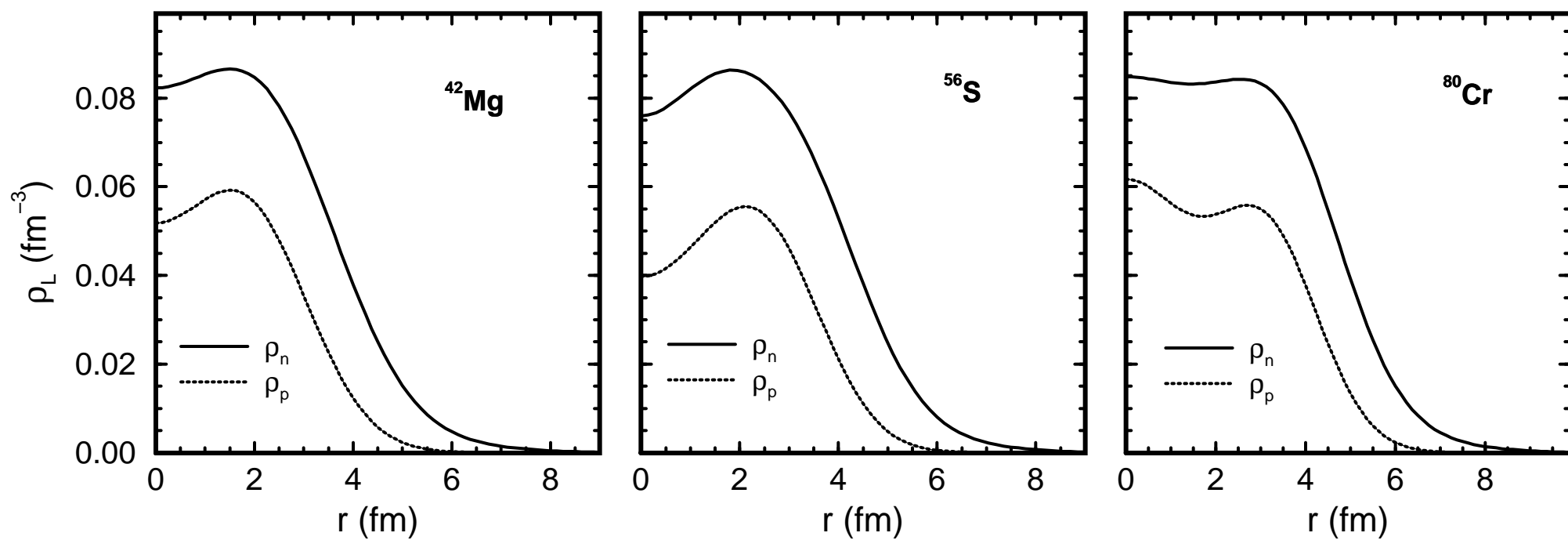


Fig. 2

Fig. 3.





**Fig. 4**

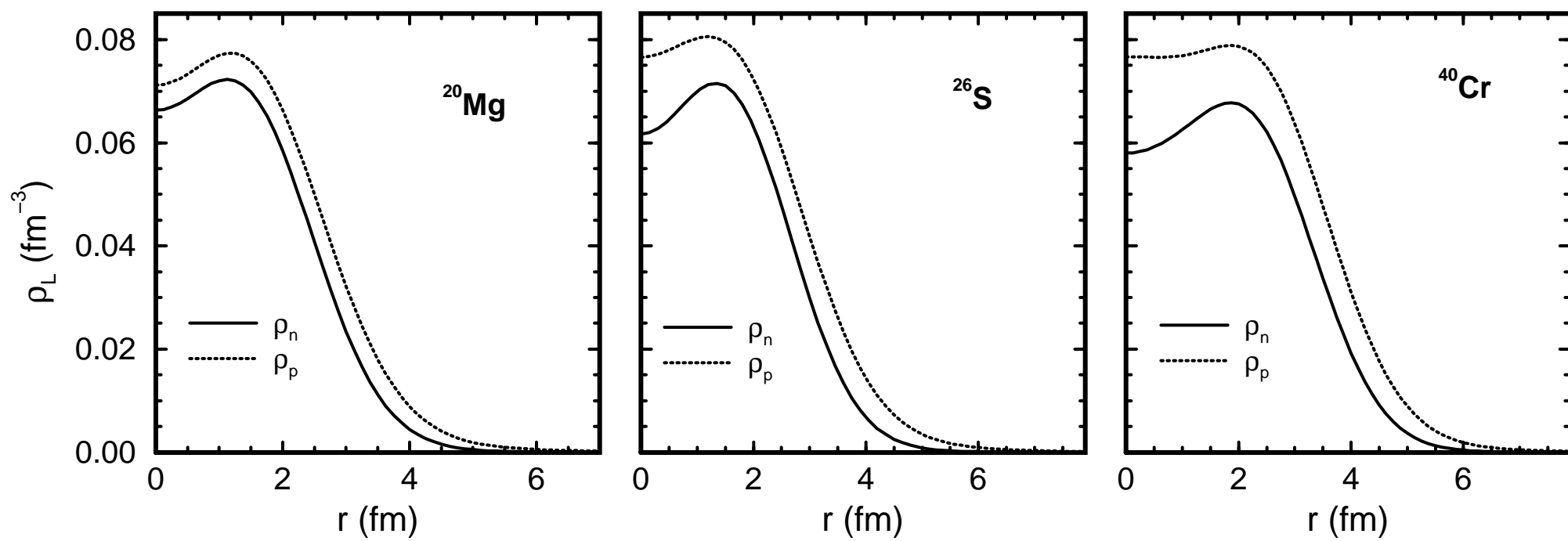


Fig. 5



Fig. 7

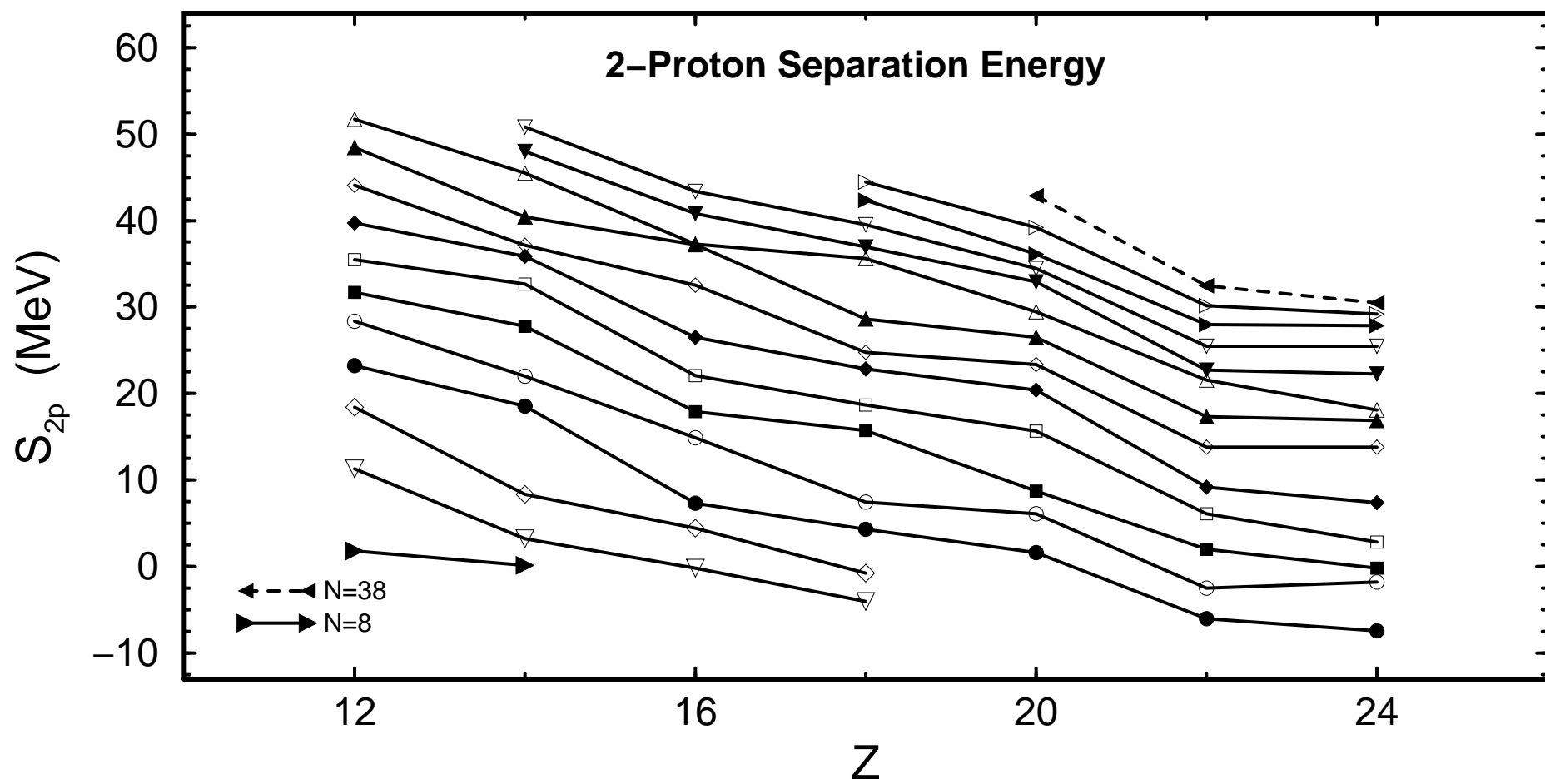
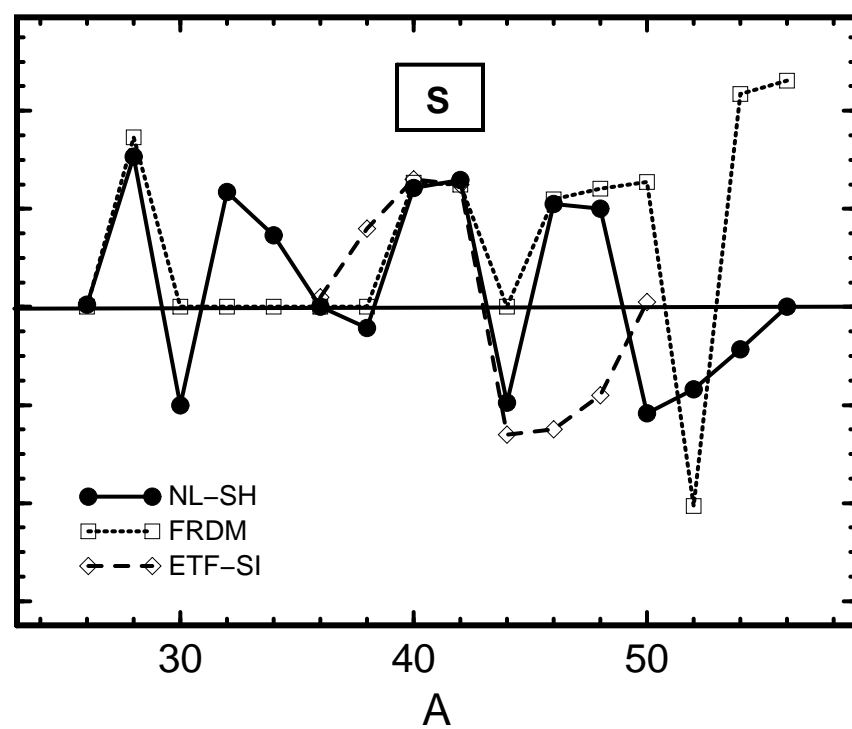
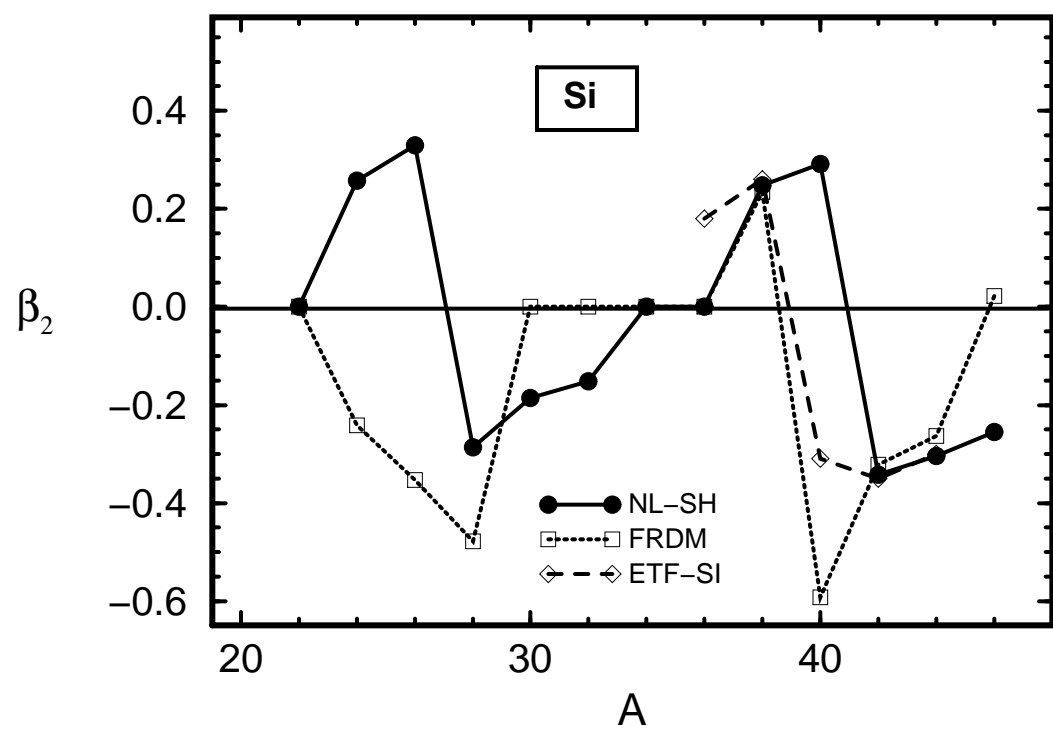
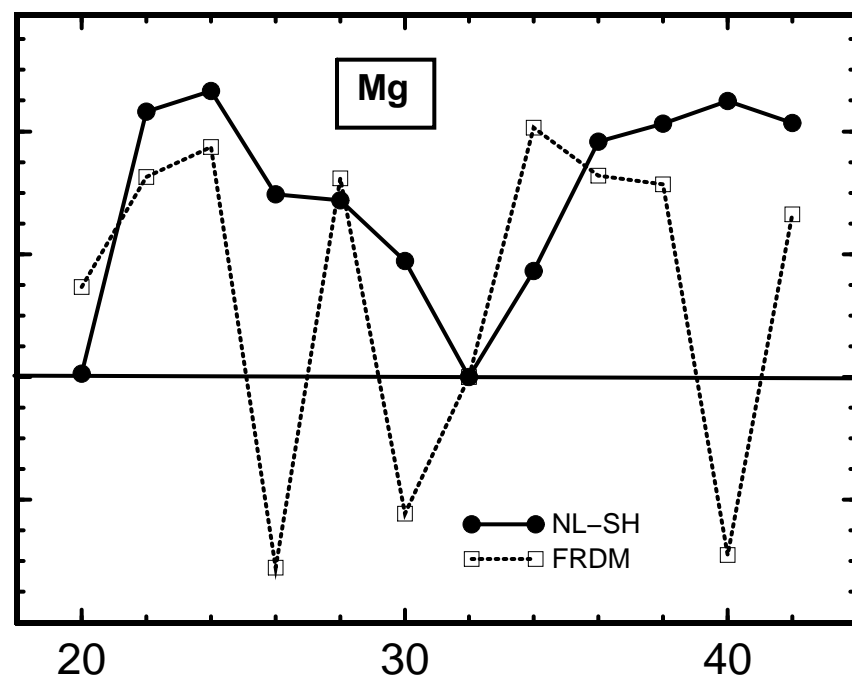
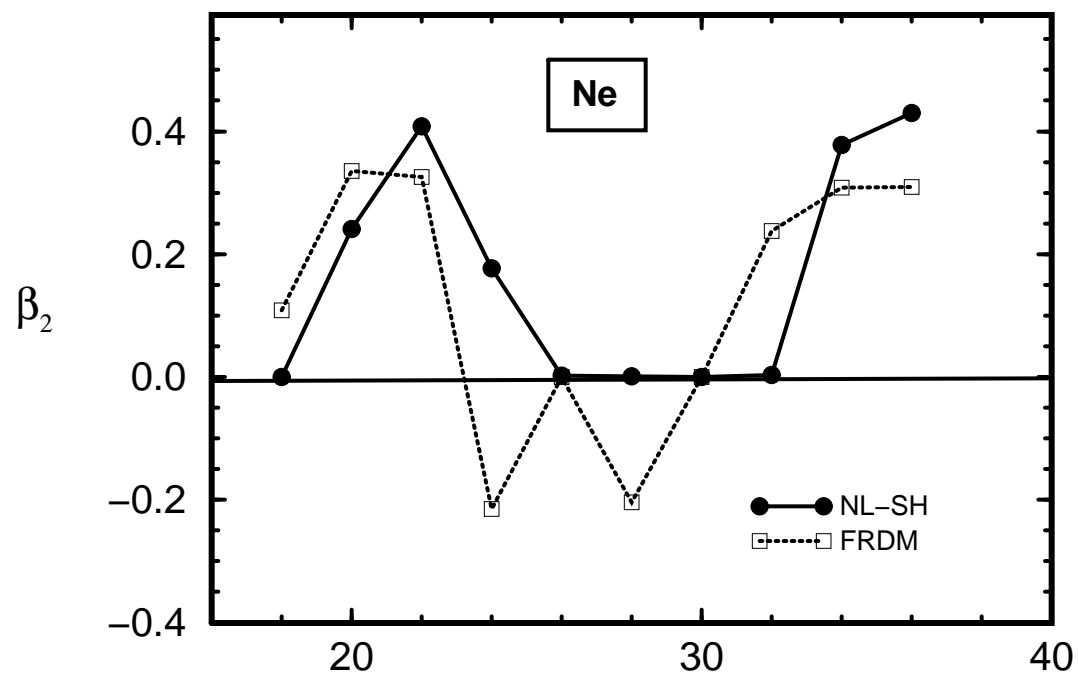




Fig. 8



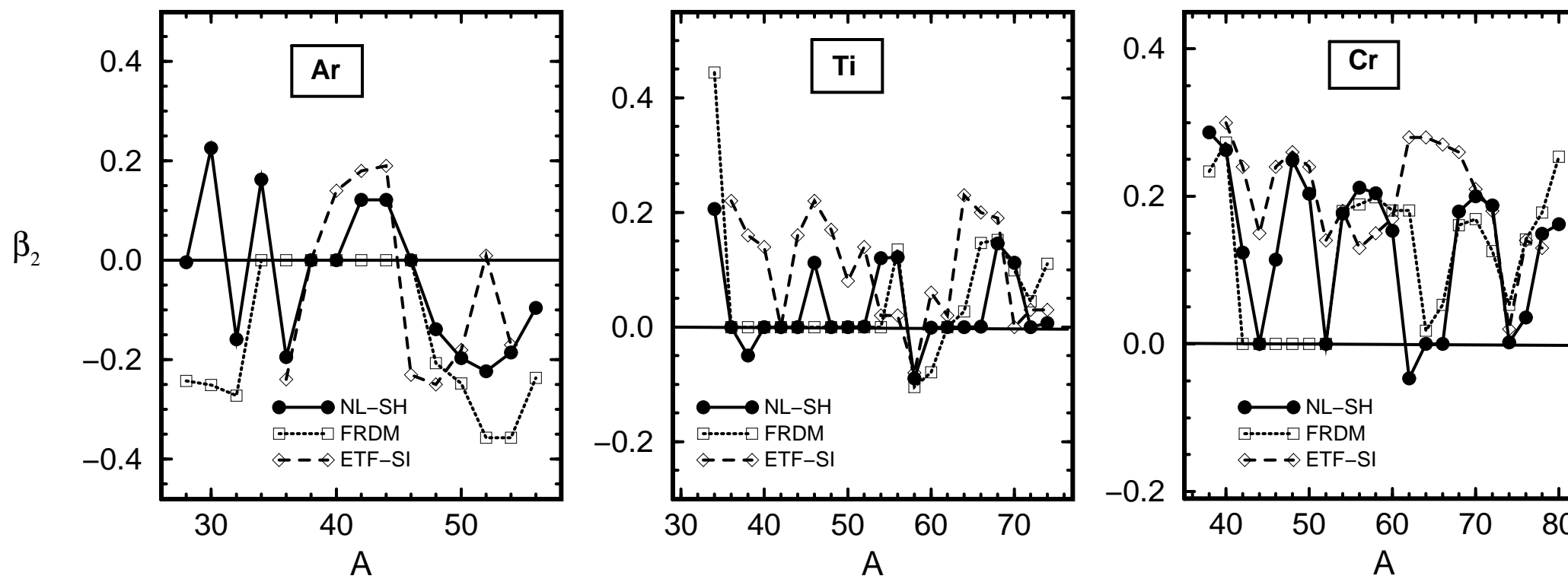
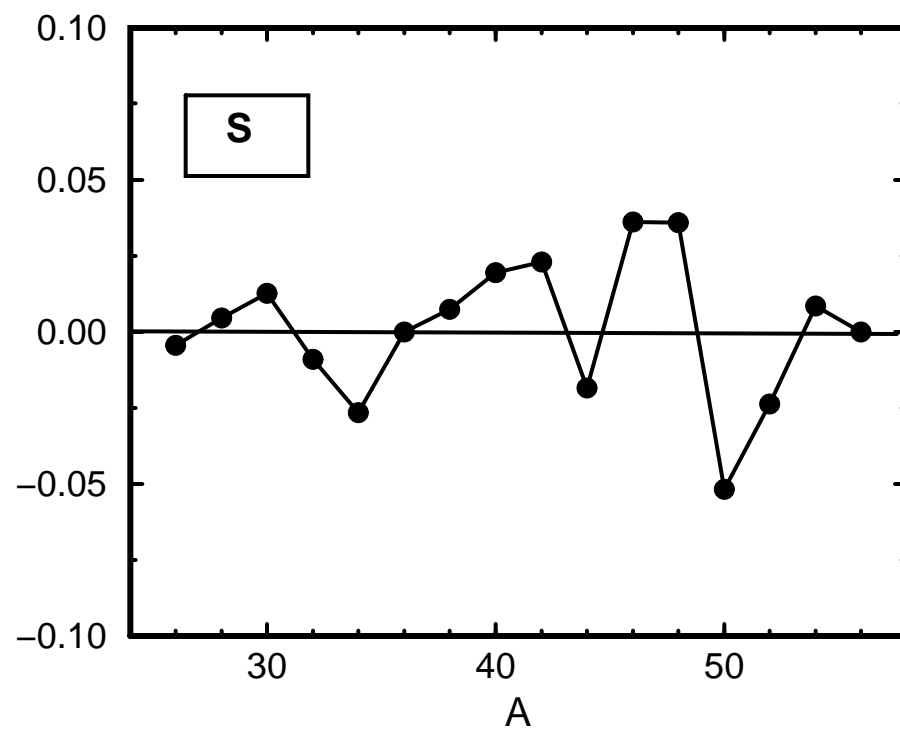
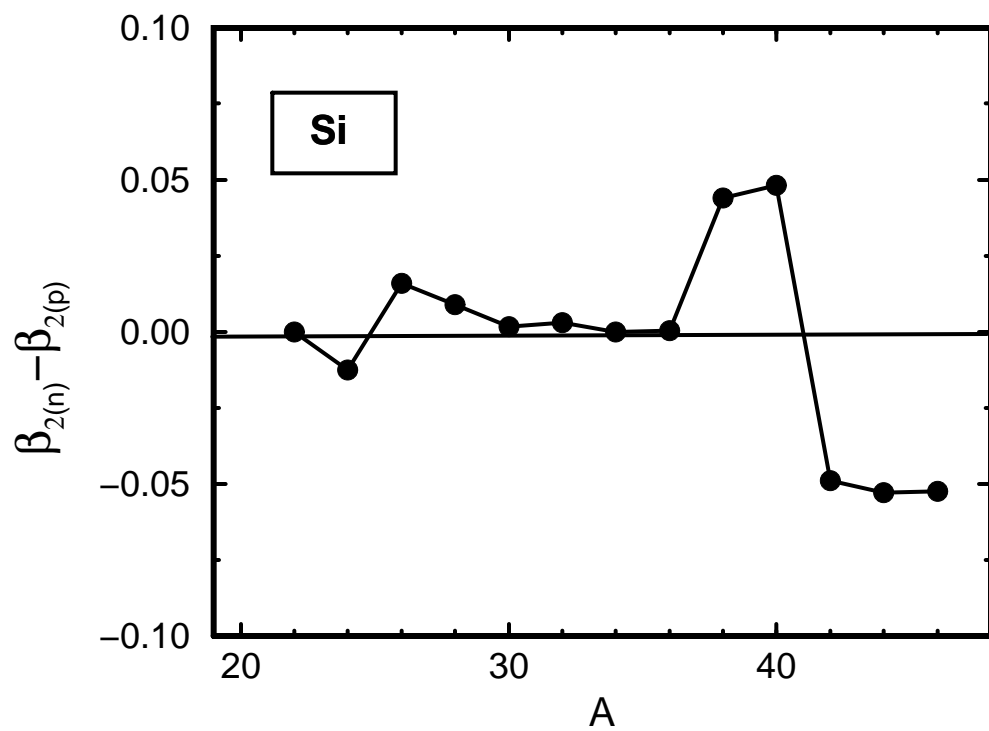
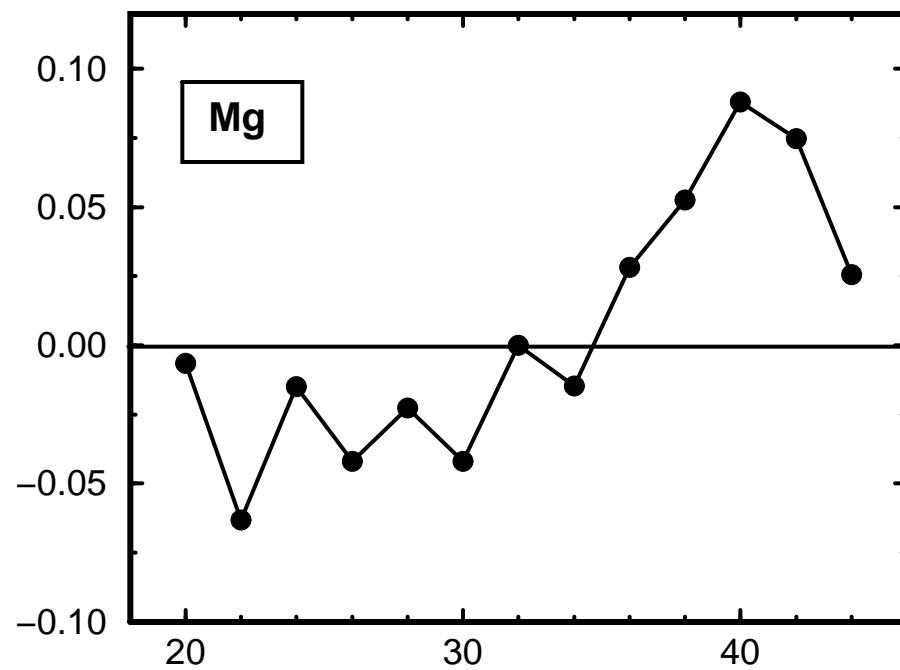
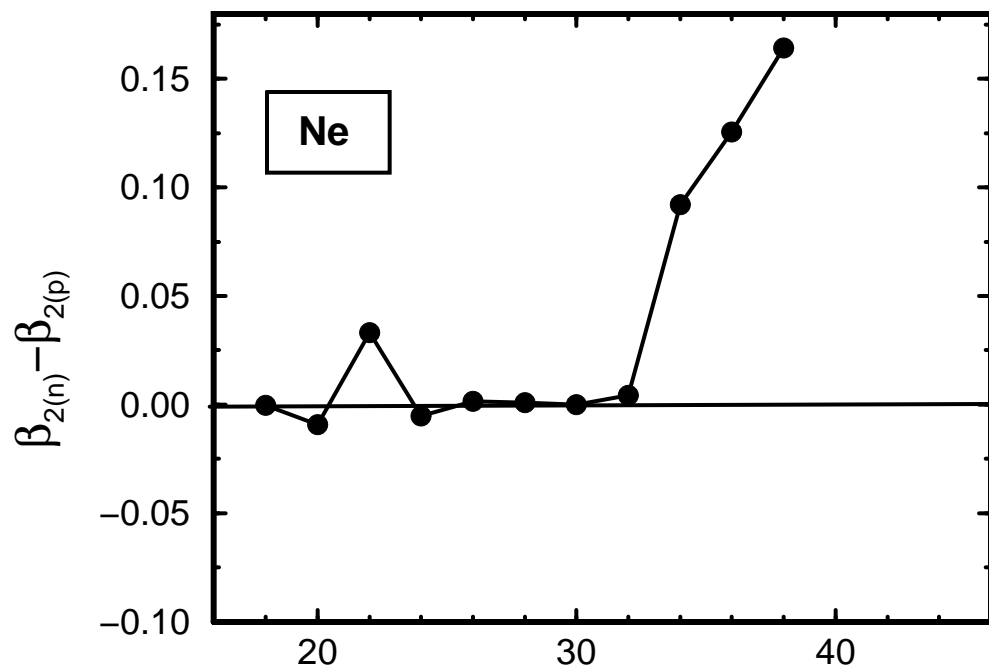


Fig. 9

Fig. 10



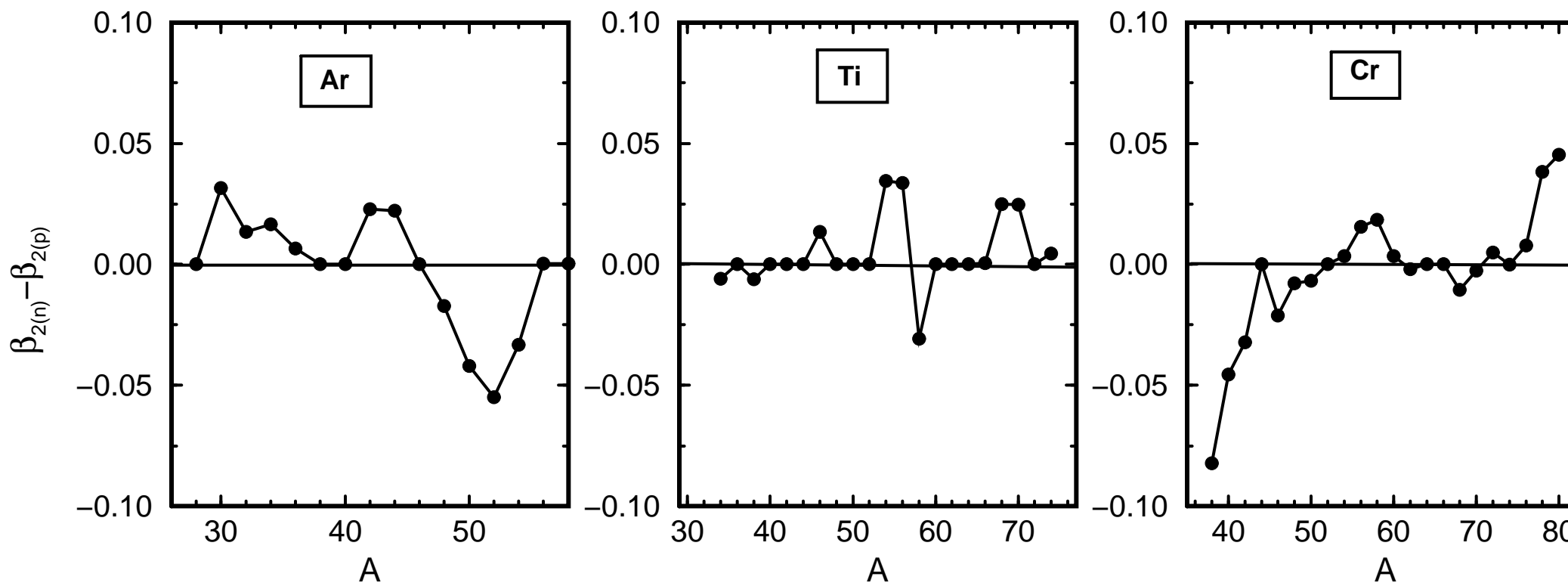


Fig. 11

Fig. 12

